PHASE-FIELD MODELING OF CRACKING IN ADDITIVELY MANUFACTURED CONCRETE

A THESIS SUBMITTED TO
THE GRADUATE SCHOOL OF NATURAL AND APPLIED SCIENCES
OF
MIDDLE EAST TECHNICAL UNIVERSITY

BY

OZAN ÖZGÜR KAYNAR

IN PARTIAL FULFILLMENT OF THE REQUIREMENTS
FOR
THE DEGREE OF MASTER OF SCIENCE
IN
CIVIL ENGINEERING

AUGUST 2023

Approval of the thesis:

PHASE-FIELD MODELING OF CRACKING IN ADDITIVELY MANUFACTURED CONCRETE

submitted by **OZAN ÖZGÜR KAYNAR** in partial fulfillment of the requirements for the degree of **Master of Science in Civil Engineering Department, Middle East Technical University** by,

Prof. Dr. Halil Kalıpçılar
Dean, Graduate School of **Natural and Applied Sciences** _____

Prof. Dr. Erdem Canbay
Head of Department, **Civil Engineering** _____

Assoc. Prof. Dr. Serdar Göktepe
Supervisor, **Civil Engineering, METU** _____

Examining Committee Members:

Prof. Dr. Kağan Tuncay
Civil Engineering, METU _____

Assoc. Prof. Dr. Serdar Göktepe
Civil Engineering, METU _____

Prof. Dr. Baki Öztürk
Civil Engineering, Hacettepe University _____

Assoc. Prof. Dr. Ercan Gürses
Aerospace Engineering, METU _____

Assist. Prof. Dr. Ferit Sait
Aerospace Engineering, Atılım University _____

Date:23.08.2023

I hereby declare that all information in this document has been obtained and presented in accordance with academic rules and ethical conduct. I also declare that, as required by these rules and conduct, I have fully cited and referenced all material and results that are not original to this work.

Name, Surname: Ozan Özgür Kaynar

Signature :

ABSTRACT

PHASE-FIELD MODELING OF CRACKING IN ADDITIVELY MANUFACTURED CONCRETE

Kaynar, Ozan Özgür
M.S., Department of Civil Engineering
Supervisor: Assoc. Prof. Dr. Serdar Göktepe

August 2023, 79 pages

This work is concerned with the computational modeling of additively manufactured concrete. Additive manufacturing involves an automated process where the product is produced layer-by-layer. One of the key advantages of this technique compared to traditional construction methods is that concrete members with complex shapes and structures can be produced easily. These tailored structures can enhance the mechanical properties of concrete such as strength and toughness considerably. Another key advantage of additive manufacturing is the high speed of construction. In this study, a new computational approach furnished with the phase-field fracture model is developed to analyze and predict the mechanical behavior of additively manufactured concrete undergoing cracking under different loading conditions. Moreover, the proposed model, validated using experimental results in the literature, is used to investigate the effect of different but scarcely used printing patterns on the cracking behavior of concrete members, particularly governed by the properties of layers and interfaces. The predictive and versatile capacity of the proposed approach is further validated through the application of the developed model to masonry walls.

Keywords: Additively Manufactured Concrete, Layered Structures, Cracking, Phase-Field Model

ÖZ

EKLEMELİ ŞEKİLDE ÜRETİLEN BETONDAKİ ÇATLAMANIN FAZ ALANI YÖNTEMİ İLE MODELLENMESİ

Kaynar, Ozan Özgür
Yüksek Lisans, İnşaat Mühendisliği Bölümü
Tez Yöneticisi: Doç. Dr. Serdar Göktepe

Ağustos 2023 , 79 sayfa

Bu çalışma, eklemeli yöntem ile üretilen betonun hesaplamalı modellenmesini konu almaktadır. Eklemeli imalat, ürünün katman katman üretildiği otomatik bir süreci içerir. Bu tekniğin geleneksel beton üretim yöntemlerine kıyasla en önemli avantajlarından biri karmaşık şekil ve yapılara sahip beton elemanlarının kolayca üretilebilmesidir. Bu özel yapılar, betonun mukavemet ve tokluk gibi mekanik özelliklerini iyileştirebilir. Eklemeli imalatın bir diğer önemli avantajı da yüksek inşa hızıdır. Bu çalışmada, farklı yükleme koşulları altında çatlayan eklemeli şekilde üretilmiş betonun mekanik davranışının kestirimi için faz-alan yöntemi ile donatılmış yeni bir hesaplamalı yaklaşım geliştirilmiştir. Ayrıca, literatürdeki deneysel sonuçlar kullanılarak doğrulanan model, pratikte yaygın olarak kullanılmayan farklı baskı örüntülerinin, özellikle katmanların ve arayüzlerin özellikleri tarafından yönetilen beton elemanların çatlama davranışı üzerindeki etkisini araştırmak için kullanılmıştır. Önerilen yaklaşımın kestirimsel ve çok amaçlı kapasitesi, geliştirilen modelin yığma duvarlara uygulanmasıyla da doğrulanmıştır.

Anahtar Kelimeler: Eklemeli Şekilde Üretilen Beton, Katmanlı Yapılar, Çatlama, Faz Alanı Modeli

To my Dear Family

ACKNOWLEDGMENTS

First and foremost, I would like to express my most profound appreciation to my advisor Assoc. Prof. Dr. Serdar Göktepe for his generous effort and guidance throughout my study. This endeavor would not have been possible without his immense knowledge and detailed advice.

I would like to sincerely thank jury members Prof. Dr. Kağan Tuncay, Prof. Dr. Baki Öztürk, Assoc. Prof. Dr. Ercan Gürses, and Assist. Prof. Dr. Ferit Sait for reviewing my study and for their valuable feedback.

I would like to express my deepest appreciation to my family. I am sincerely grateful to my dear mother, Kadriye Kaynar, my father, İrfan Kaynar, and my sisters, Deniz and Özgenur Kaynar, for their immeasurable support and love.

I want to thank my roommate Norgen Muka for his friendship and support. Our discussions about a wide range of topics have greatly broadened my perspective on science and life.

I would like to truly thank my Middle East Technical University fellows and friends Pınar Arıkoğlu, Mustafa Çelik, Gamze Muratoğlu, Baki Aykut Bilginer, Sinan Fırat Dal, Özgür Paşaoğlu, Muhittin Babaoğlu, Ali Fatih Kuloğlu, and Batuhan Kalpakçı for their presence and support.

Lastly, I gratefully acknowledge the funding for my Master of Science study from the Scientific and Technological Research Council of Turkey (TUBITAK) under the 2210-A National MSc Scholarship Program.

TABLE OF CONTENTS

LIST OF TABLES

TABLES

LIST OF FIGURES

FIGURES

LIST OF SYMBOLS

d, ∇d, Δd	Crack phase-field, its gradient and Laplacian
α	Geometric crack function
Γ, Γ_l	Sharp and regularized crack surfaces
l	Length scale
c_0	Scaling parameter for geometric crack function
γ	Crack density function
g	Degredation function
Ψ	Free energy function
λ, μ	Lamé constant and shear modulus
$\boldsymbol{u}$	Displacement field
$\boldsymbol{\varepsilon}$, $\boldsymbol{\sigma}$	Strain and stress tensors
$\mathcal{E}$, $\mathcal{D}$, $\mathcal{P}$	Free energy, dissipation, and external power functionals
Φ	Dissipation function per unit volume
$\bar{\boldsymbol{b}}$, $\bar{\boldsymbol{t}}$	Body force and traction
g_c	Fracture energy per unit area
E, ν	Elasticity modulus and Poisson's ratio
σ_c	Critical stress
Ψ_c	Critical fracture energy per unit volume
$\mathcal{H}$	History field
ζ	Driving force slope
h	Effective mesh size

CHAPTER 1

INTRODUCTION

In this study, the computational modeling of additively manufactured concrete possessing layered structure is investigated. To examine the mechanical behavior of additively manufactured concrete, including fracture, a framework of governing mechanical equations coupled with the phase-field formulation is described. Then, this framework is applied to representative numerical examples to demonstrate the capabilities of the model. In this chapter, the motivation and the problem description of the study are provided. Later, the existing studies from the literature are reviewed. Finally, the scope and outline of the thesis are given.

1.1 Motivation

In the general context, additive manufacturing (AM) is an automated process where the product is manufactured layer-by-layer. The field of additive manufacturing has witnessed remarkable advancements in recent years, revolutionizing various industries such as manufacturing, medicine, and construction with its different types of technologies, namely vat polymerization, powder bed fusion, material jetting, binder jetting, direct energy deposition, sheet lamination, and material extrusion [1]. One of the most significant applications of additive manufacturing technology in construction is the fabrication of concrete structures by an extrusion-based system as shown in Figure 1.1 adopted from [2]. Additively manufactured concrete, also known as 3D printed concrete, offers unique opportunities for architects, engineers, and designers to create complex, customized, and sustainable structures. This emerging technology has the potential to transform the construction industry by enabling faster construc-

Figure 1.1: Printing of additively manufactured concrete (Wolfs et al. [2]).

tion, reducing material waste, and providing greater design freedom. However, there are also some disadvantages of additively manufactured concrete. For example, additively manufactured concrete requires excessive use of cement and causes high CO_2 emissions. Furthermore, because of its additive manufacturing process, additively manufactured concrete structures contain interfaces weaker than the material itself, which may affect the mechanical behavior adversely.

1.2 Problem Description

Despite the increasing interest in additively manufactured concrete, its successful implementation requires a deep understanding of the material behavior, printing processes, and structural performance. Computational modeling allows researchers to simulate and analyze various aspects and plays a pivotal role in gaining insights into the complex interactions involved in the additive manufacturing of concrete. One of the aspects that need to be considered regarding the successful implementation of additively manufactured concrete is the mechanical behavior of additively manufactured concrete involving cracking. Since additively manufactured concrete possesses a layered structure, it shows anisotropic behavior. Furthermore, the interfaces between

layers are weaker than the material itself regarding structural performance. Therefore, to increase the overall toughness of the additively manufactured concrete, the structure of the interfaces should be addressed. However, there are a limited, if any, number of studies existing in literature modeling the mechanical behavior, including cracking in additively manufactured concrete computationally.

1.3 Literature Review

In this section, we review the existing body of knowledge from the literature around the scope of the thesis, focusing on several aspects: phase-field modeling, fracture behavior of layered materials, analytical approaches to layered structures, additively manufactured structures, and experimental studies on additively manufactured concrete.

1.3.1 Phase-Field Modeling

Fracture is a fundamental and complex phenomenon in various engineering and material science applications, ranging from the failure of structural components to the propagation of cracks in brittle and ductile materials. The ability to accurately model and predict fracture behavior is crucial for ensuring the integrity and reliability of structures. Over the years, the phase-field modeling of fracture has emerged as a promising computational technique for simulating fracture processes due to its ability to capture crack initiation, propagation, and branching in a computationally efficient manner.

In the past two decades, the phase-field method has gained recognition as an efficient approach for simulating fracture in computer-based simulations. This method has been widely applied and expanded across various fields, including brittle fracture [3–10], ductile fracture [11–13], cohesive fracture [14–17], dynamic fracture [18–23], finite deformation fracture [24–27]. These applications highlight the versatility and broad utility of the phase-field method in addressing fracture-related phenomena across a wide range of fields.

The decomposition of elastic energy and fracture energy into tensile and compressive parts is a widely used method to differentiate between tensile and compressive damaging modes. Miehe et al. [5] established a thermodynamically consistent phase-field brittle fracture model in both rate-independent and viscous over-force settings to overcome the problems such as the modeling of discontinuities and unrealistic crack patterns resulting from the energy degradation in both tension and compression. They additively split the strain energy into tensile and compressive parts by using the spectral representation of the strain tensor. Following this work, in [6], they introduced an operator split algorithm for a staggered update of the local history field maximum reference energy obtained in the deformation history driving the evolution of the fracture. Miehe et al. [26] extended this framework to model the fracture in thermo-mechanical and multi-physics problems at finite strains. In order to avoid damage-type degradation at low stresses, the fracture contribution to the "total" pseudo-energy with threshold is defined. They also introduced length-scale independent driving forces by expressing critical energy release rate for driving force without threshold and energetic threshold for driving force with threshold length-scale dependent. Another strain energy decomposition method is used by Amor et al. [7] who applied decomposition to the strain energy using the volumetric and deviatoric contributions of the strain tensor to prevent unrealistic crack patterns and cracking in compression.

The decomposition of the elastic energy into parts results in a strongly non-linear constitutive relation and makes the computational cost of the formulation extremely high. To address this issue, Ambati et al. [28] proposed the so-called Hybrid formulation where the stress expression is derived from the free energy function while the driving force is derived from only the tensile part of the free energy. They also established a stopping criterion for the staggered scheme to decrease computational costs by using larger loading increments. Wu [29] also proposed a similar Hybrid formulation where the stress expression is derived from the free energy function while the driving force is expressed in terms of the major principal value of the effective stress.

Other than the spectral decomposition and the volumetric-deviatoric decomposition, Steinke and Kaliske [30] proposed an approach called the directional decomposition where the stress tensor is decomposed with respect to crack orientation. The model is

based on the additional information on the crack orientation, which enables a decomposition of stresses with respect to a local crack coordinate system into crack driving and persistent components.

1.3.2 Fracture Behavior of Layered Materials

Layered materials have interfaces where either a crack deflects or penetrates, depending on the strength and toughness differences between two materials through which the crack passes. Crack deflection helps the toughening of the material because of the increase in energy dissipation, while crack penetration results in little or no toughening in the material. Therefore, the properties of the interfaces play a major role in the layered materials [31]. Nguyen et al. [16] modeled interfaces continuously in complex microstructures throughout the domain by describing both the bulk crack density and the interface crack density with the phase-field. With this formulation, both crack types simply interact with each other. Numerical examples were performed on microstructures obtained by microtomography, including concrete microstructures, and concluded that the model can be successfully used to study microcracking in composite materials where both interfacial damage and matrix crack propagation occur.

The fracture of layered heterogeneous materials is a complex phenomenon, and crack-interface interaction can be modeled in several ways to investigate different types of interfaces in layered media. Nguyen et al. [32] used zero thickness perfectly bonded interfaces and cohesively bonded interfaces and also sharp and regularized transition zones through interfaces to investigate influences of material mismatch, interfacial properties, and loading conditions on fracture of layered materials for 2D and 3D models. They could capture different crack paths, specifically crack penetration and branching, depending on these effects as the crack passes through the interface. They also showed that the interface models and transition zone highly affect the crack paths and damage mechanism. Paggi and Reinoso [33] used cohesive interfaces in the phase-field model to investigate the competition of crack penetration and crack deflection at an interface. This investigation was made by analyzing the role of the fracture toughness ratio between the interface and the bulk material.

Interfaces can also be modeled as discrete bodies having finite thicknesses. Hansen-

dörr et al. [34] used this type of interfaces to investigate interface failure in brittle materials. Due to the interaction between bulk material and interface material, the fracture toughness of the interface material is not fully responsible for the crack at the interface. Therefore, they lowered the interface fracture toughness by using a compensation procedure in order to properly compensate for the influence of the fracture toughness of the bulk material. However, in this study, only the sharp transition of the fracture toughness between layers was considered.

Kuhn and Müller [35] investigated the fracture of heterogeneous materials by using the adaptation of configurational forces to the phase-field model. They analyzed layered materials with different elastic modulus and/or fracture resistance and materials having sinusoidal variations of elastic modulus and/or fracture resistance. Crack jumps at interfaces occurred in both types of structures.

1.3.3 Analytical approaches to layered structures

There are analytical approaches to quantify the properties, such as the toughness of layered structures. The fracture and toughening mechanisms of layered materials were first investigated analytically by Ming, Suo, and Hutchinson for materials subjected to axial loading and bending, see [36–38]. Following these studies, Li et al. [39] investigated delamination in layered materials subjected to shear. Leguillon and Martin [40] studied the strengthening effect of the layered structures because of the elastic modulus mismatch of the layers. They analyzed the mechanisms of the crack-crossing interface by considering the three-point bending test of the bimaterial layered beam. Following this work, Leguillon and Martin [41] analyzed the same effect in a homogenous beam embedding a stiffer thin layer. They stated that as the number of layers increases, the strengthening increases, converging to a finite value as the number of layers is infinite.

The contrast in the fracture toughness of the layers can also have an influence on strengthening and toughening, as in the case of elastic contrast. Hossain et al. [42] developed a method to determine the effective toughness of heterogeneous materials by discussing their differences with respect to homogeneous materials. They achieve this by solving the microscopic problem subjected to the so-called surfing boundary

conditions. They concluded that the heterogeneity may increase the overall toughness of the structures due to the difference between fracture toughness and elastic moduli of the constituent materials. Following this work, Hsueh et al. [43] discussed the reasons for this phenomenon. They deduced that stress fluctuations throughout the heterogeneous body and renucleation of the crack because of the encounter of the crack with a stiff material are the major reasons resulting in toughening of the structure. They investigated the effect of both separately by using appropriate geometric setups. Brach et al. [44] extended these works to the anisotropic setting by considering the propagation of the crack at various angles to the layers. They studied two situations where the toughness or the elastic modulus alternates throughout the layers. In the first situation, the overall toughness is equal to the toughness of the tougher material independent from the angles of crack propagation, except the crack propagates along with the interface where the toughness of the material with the low toughness governs. In the second case, the toughening depends on the angle of crack propagation decreasing as the direction of propagation deviates from the normal to the layers.

1.3.4 Additively Manufactured Structures

Because of their additive manufacturing process, additively manufactured structures are composed of layers. Therefore, as layered structures, their interfaces and orientation of the layers highly affect the mechanical properties. Li et al. [45] investigated additively manufactured structures by using anisotropic elastoplastic phase-field modeling. They used two phase-field variables, one for bulk damage and one for interfacial damage, to identify the crack initiation and propagation in the interface and bulk of the elastoplastic structures. Following this work, Li et al. [46] focused on the topology and orientation of the layers to achieve fracture resistance improvement on additively manufactured elastoplastic structures. They proposed an optimization process maximizing their fracture resistance by considering both the orientation of the layers and the topology of the structure.

The additive manufacturing of concrete is an emerging automated construction technology enabling the production of concrete structures layer-by-layer at high speed.

Xiao et al. [47] studied the anisotropic behavior of 3D printed concrete, including interfacial properties, by using finite element analysis. The compressive and flexural strengths were measured to investigate the effect of nozzle dimensions, interfacial bond strength, and concrete properties. When the tangential direction of the interface is aligned with the direction of the lateral expansion of the specimen due to compression, the compressive strength becomes lower since the relative slip of the interface is larger. When the tangential direction of the interface is aligned with the tensile direction of the mid-span of the specimen, the flexural strength significantly reduces due to the effect of the interfacial properties. These effects can be mitigated significantly by increasing the nozzle dimensions and interfacial bond strengths.

1.3.5 Experimental Studies on Additively Manufactured Concrete

There are experimental studies in the literature quantifying the mechanical properties and investigating the printing, material, and structural parameters of additively manufactured concrete. Daungwilailuk et al. [48] studied additively manufactured concrete walls experimentally and by using finite element analysis. They analyzed a flat wall with a truss in the inner part of the wall and a wall with the shape of a diamond on the outer surface. The pits of the diamond pattern were exposed to larger stress, causing the cracks and spalling of the concrete. The truss in the flat wall helped to prevent the bowing and buckling of the specimen. Wolfs et al. [2] examined the flexural strength and tensile splitting strength of additively manufactured concrete specimens with different layer orientations along with the reference conventionally cast concrete. They found that layer orientation has an effect on flexural strength but little effect on tensile strength. However, for all orientations of the additively manufactured concrete, the tensile splitting strength was lower compared to the reference conventionally cast specimen. They also investigated the effect of the interval time between the printing of two layers. Both the flexural and tensile splitting strength of the specimens decreased as the interval time increased.

Because of their layered structure, additively manufactured concrete specimens show anisotropy. This anisotropic behavior may also be affected by the printing patterns. Murcia et al. [49] examined this effect by quantifying compressive strength and the

modulus of elasticity of the additively manufactured concrete specimens having different printing patterns. They found that additively manufactured concrete has significant anisotropy in the direction perpendicular to the layers independent of the printing pattern. This shows the transversely isotropic behavior of additively manufactured concrete specimens. They also compared additively manufactured concrete specimens with the conventionally cast ones and showed that additively manufactured concrete specimens have higher compression strength than that of conventionally cast concrete specimens except in the direction perpendicular to the layers. Le et al. [50] examined compressive strength, flexural strength, and tensile bond strength of fiber-reinforced additively manufactured concrete having different geometries. The curvy-shaped-full-scale bench structure showed up to 30% less compressive strength compared to the specimens extracted from straight-line printed slabs. Moreover, the tensile bond strength decreased as the interval of the printing gap increased. When the tension was aligned with the filaments, flexural strength increased by approximately 50% compared to the case where the tension was perpendicular to the layers. The presence of fibers affects the anisotropic properties of the additively manufactured concrete. Ding et al. [51] investigated this by examining additively manufactured concrete reinforced with polyethylene fibers under flexure. The specimens were loaded in different directions with respect to layers compared with each other, along with the specimens without fibers. The number of cracks was higher for the specimens with fibers than those without fibers. There was no crack propagation along the layer interface for the specimens with fibers. The flexural strength – displacement curves of the specimens are compared with the mold-cast specimens. When the fiber ratio was increased and fiber orientation became more uniform, the flexural strength became greater. However, despite the increased fiber ratio and uniformly aligned distribution of the fibers, 3D specimens showed many different types of behavior with respect to different directions, showing that the anisotropy of the specimens is still preserved. The orientation of steel fibers affects the mechanical performance of the additively manufactured concrete. However, while printing, the orientation of steel fibers may differ under certain conditions. Arunothayan et al. [52] examined the effect of extrusion nozzle size, printing speed, and fiber volume fraction on the orientation of the fibers. It was found that the smaller nozzle size and higher fiber ratio considerably improved the parallel alignment of the fibers to the printing direction and consequently

increased the mechanical performance of the specimens significantly.

Because of the layered nature of the additively manufactured concrete members, they have lower strength at the interfaces. To address this issue, Zareiyan et al. [53] suggested interlocking interfaces between layers to increase the interlayer strength. They performed tensile splitting and compression tests and concluded that with an optimum size of interlock, the strength of the members can be increased considerably. Following this work, He et al. [54] developed a tooth-like interface for a similar purpose. They found that the tooth-like interface increases the tensile and shear strength of the members considerably and makes the interface behave more cohesively. However, in these studies, only a limited number of interface types are investigated, no load-displacement performance of the specimens is provided, and the effects on the toughness of these interfaces are not discussed.

The formation of weak interfaces between layers during deposition is an important issue of additively manufactured elements. Nerella et al. [55] analyzed the layer-interface properties of additively manufactured concrete elements by investigating the influence of binder composition and time interval between the deposition of layers. They measured the flexural strength and compressive strength of the printed parts and showed that the direction of loading has a lower dependency on the elements prepared with the mixture containing high amounts of supplementary cementitious materials than those containing solely Portland cement. Also, the former ones have a more homogenous microstructure and lower anisotropy than the latter ones. A decrease in the strength due to the increase in layer interval time is more distinguishable in the former one in the flexural strength test.

The materials based on structures from nature have aroused interest recently. These bioinspired materials may enhance the mechanical properties of engineering materials. Pham et al. [56] studied the flexural and compressive strength of additively manufactured concrete members with and without fibers having different printing patterns, including unidirectional and multidirectional patterns. The results show that patterns formed from the bioinspired Bouligand structures and the presence of fibers may increase the flexural and compressive strength of the additively manufactured members considerably.

The extrusion parameters, such as the shape of the nozzle dimensions, layer height, nozzle direction, and scraper, may affect the mechanical performance of the additively manufactured concrete. Ji et al. [57] investigated the effects of nozzle direction and scrapers on the buildability, mechanical properties, and microstructure of additively manufactured concrete. Vertical nozzle direction compared to horizontal nozzle increased the mechanical properties; however, it decreased the buildability of additively manufactured concrete. The interlayer porosity of the member printed by the vertical nozzle is 20.2% less than that printed by the horizontal nozzle. The vertical nozzle with scrapers decreased porosity up to 30% and increased flexural strength up to 50% compared to that without scrapers.

To increase the load-bearing capacity of the additively manufactured concrete structures, reinforcement strategies that are compatible with extrusion-based printing are being developed. Gebhard et al. [58] investigated experimentally additively manufactured concrete beams with various types of reinforcement under 4-point bending tests. They obtained crack patterns by using digital image correlation and concluded that the brittle failure was observed in unbonded post-tensioned reinforced beams with few bending cracks. On the other hand, the beams with longitudinal reinforcement experienced both bending and shear types of cracks. The effect of fiber reinforcement on the mechanical performance of the additively manufactured concrete members is investigated by Pham et al. [59] with steel fibers and by Ma et al. [60] with basalt fibers. Xiao et al. [61] studied the flexural performance of additively manufactured concrete reinforced with steel cables in different directions. The steel cables were placed in the direction perpendicular to the interfaces, and these specimens showed no significant anisotropy under flexure. Liu et al. [62] studied the additively manufactured concrete specimens with steel wire mesh reinforcement and concluded that steel wire mesh reinforcement changes the brittle failure mode to ductile mode and increases the bending strength considerably. However, some of the strategies listed here limit the feature of being an automated process and the ability to enable fast construction of additive manufacturing technology.

There are studies in literature performing mechanical characterization on additively manufactured concrete. Heever et al. [63] evaluated the material parameters by the procedures of direct tension, uniaxial compression, and four-point bending tests.

However, in this study, only fiber-reinforced specimens were investigated, and the characterization of unreinforced plain additively manufactured concrete was not performed. Kruger et al. [64] evaluated the Poisson ratio of the additively manufactured concrete, and they found that the Poisson ratio is 0.21 with horizontal interlayers, 0.24 with vertical interlayers.

One of the concrete-like materials that are investigated for additive manufacturing applications is engineered cementitious composites. Engineered cementitious composites (ECC) are fiber-reinforced composites that have enhanced mechanical properties. Zhu et al. [65] investigated the bending behavior of ECCs having different geometrical structures. The results showed that using ECC as a base material increased the ductility of the specimens while changing the geometrical configurations of the specimens by using different printing paths highly affected the ultimate load of the specimens. Zhang et al. [66] investigated ECCs in compression and flexural tests and showed that the strength of the members is higher when the filaments are perpendicular to the loading direction than when those are parallel to the loading direction.

1.4 Aim and Scope of the Thesis

The aim of this study is to model the mechanical behavior of additively manufactured concrete structures that undergo cracking. To achieve this, we propose a phase-field model that takes into account the layered structure of the additively manufactured concrete. We aim to show that by using different geometrical configurations of the layers and interfaces, the overall toughness of the structures can be increased. The studies on additively manufactured concrete are restricted to mainly experimental studies, and in this study, we propose a computational model in light of these experimental studies. The fundamental concepts and novel aspects of this thesis are

- Developing a robust computational model for the mechanical behavior of additively manufactured concrete undergoing cracking
- Modeling the interfaces of additively manufactured concrete by using different material parameters

- Generating different geometrical configurations of the layers and interfaces to investigate their effects on the mechanical performance of additively manufactured concrete.
- Extending the proposed approach to model the fracture behavior of masonry walls under various loading and boundary conditions

1.5 Outline of Thesis

The rest of the thesis is organized as follows. Chapter 2 focuses on the formulations related to phase-field models in the context of computational modeling of brittle fracture.

Chapter 3 is dedicated to the numerical formulation of the governing equations. The chapter begins with the derivation of the weak form of the governing equation using the Galerkin method. Next, the spatial discretization by the Finite Element Method is presented. Finally, within the iterative solution procedure of the Newton method, the solutions of the coupled finite element equations are obtained by a staggered scheme.

In Chapter 4, the representative numerical analyses to examine the validity and accuracy of the model in understanding the mechanical behavior of additively manufactured concrete are conducted. The chapter includes convergence analyses to ensure the objectivity of the models. Next, the model is applied to representative numerical examples to investigate the mechanical behavior of additively manufactured concrete with various layer configurations. The proposed approach is further applied to masonry walls to analyze their failure characteristics under different loadings.

Finally, Chapter 5 presents the conclusions drawn from the validated and generated models for additively manufactured concrete. The chapter summarizes the key findings and insights obtained from the computational modeling and analysis conducted in earlier chapters. Furthermore, possible future extensions are outlined.

CHAPTER 2

PHASE-FIELD APPROXIMATION OF THE CRACK TOPOLOGY

2.1 One-dimensional bar with a crack

For the theoretical explanation of the phase-field theory in the context of diffusive crack topology, first, we consider an infinitely long one-dimensional bar of cross-section Γ and length $\mathcal{L} \subset [-\infty, +\infty]$ occupying the domain $\mathcal{B} = \Gamma \times \mathcal{L}$ with position $x \in \mathcal{L}$ on its axis. The bar also contains a crack in the middle where $x = 0$ and Γ represents the fully-broken crack surface (Miehe et al. [5]). A scalar field variable $d(x) \in [0, 1]$ is defined to describe this crack topology. When $d = 0$, the material is said to be unbroken and when $d = 1$, the material is said to be fully-broken. The auxiliary field $d(x)$ is denoted as the crack phase-field. In the present problem of sharp crack topology, the crack phase-field is equal to 1 at $x = 0$ and it is equal to 0 elsewhere. The sharp crack phase-field can be approximated to a diffusive crack phase-field by the exponential function

$$d(x) = e^{-|x|/l} \,. \tag{2.1}$$

The function regularizes the crack over the axis of the bar with the property $d(0) = 1$ and $d(\pm\infty) = 0$. The regularization is governed by the value of the scalar variable the so-called length scale l. As l approaches to 0, a diffuse crack converges to a sharp crack. The diffuse crack topologies for different values of the length scale l along with the sharp crack topology are given in Figure 2.1. Furthermore, it is observed that (2.1) is the solution of the homogeneous differential equation

$$\alpha'(d) - 2l^2 d_{,xx} = 0 \quad \text{where} \quad d_{,xx} = \frac{\partial^2 d}{\partial x^2} \quad \text{with} \quad \alpha(d) = d^2 \tag{2.2}$$

with the Dirichlet-type boundary conditions $d(0) = 1$ and $d(\pm\infty) = 0$ and the evo-

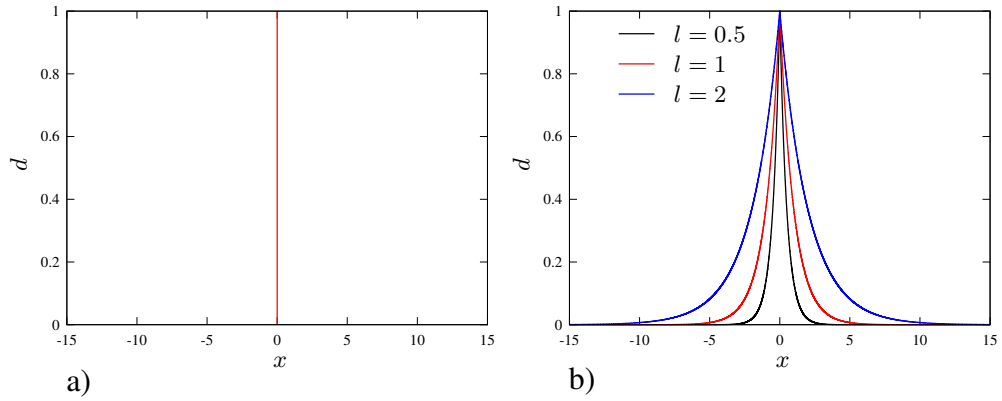

Figure 2.1: Crack topologies. a) A sharp crack at $x = 0$. b) Diffuse cracks with different values of the length scale.

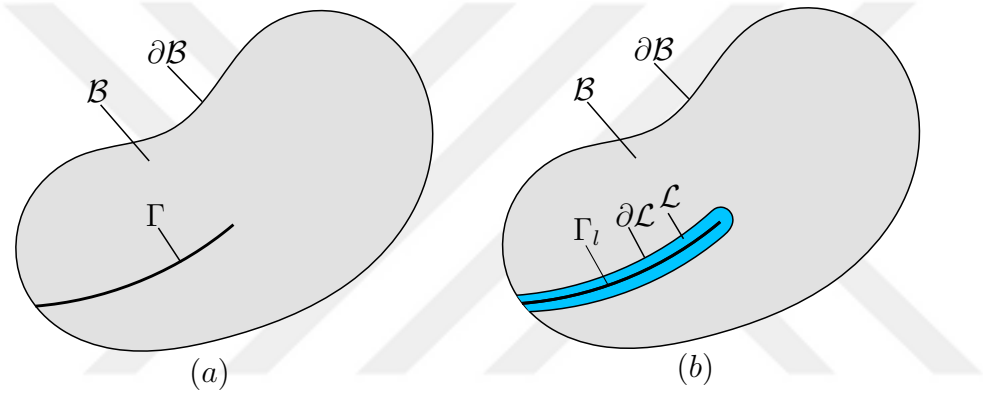

Figure 2.2: Crack topologies. Solid $\mathcal{B}$ with (a) the sharp crack surface, and (b) the regularized crack surface.

lution of the phase-field is controlled by the geometric crack function $\alpha(d)$. Furthermore, the differential equation (2.2) is the Euler equation of the variational principle

$$d = \text{Arg}\{\inf_{d \in W} I(d)\} \quad \text{with} \quad W = \{d | d(0) = 1, d(\pm\infty) = 0\}\,. \tag{2.3}$$

Integrating the Galerkin-type weak form of (2.2) results in

$$I(d) = \frac{1}{c_0}\int_{\mathcal{B}} \left[\alpha(d) + l^2 (d_{,x})^2\right] dV \tag{2.4}$$

where c_0 is a scaling parameter. Using $dV = \Gamma dx$ and the approximate solution of the crack phase-field, one can obtain that

$$\Gamma_l(d) := \frac{1}{l} I(d) = \frac{1}{c_0 l}\int_{\mathcal{B}} \{\alpha(d) + l^2 (d_{,x})^2\} dV\,. \tag{2.5}$$

The minimization of this scaled functional also gives the regularized crack topology depicted in Figure 2.2 when the body is fully-degraded.

2.2 Crack Surface Density Function

The one-dimensional setting considered above motivates us to extend the concept of a diffusive crack topology to multi-dimensional solids. Consider that $\mathcal{B} \subset R^{\delta}$, is the reference configuration of a material body and $\partial\mathcal{B} \subset R^{\delta-1}$ is its surface with dimension $\delta \in 1, 2, 3$ in space. The evolution of cracks in time is the point of interest. Therefore, the crack phase-field is defined to study crack propagation in the range $\mathcal{T} \subset R$ of time as

$$d = \begin{cases} \mathcal{B} \times \mathcal{T} & \to [0,1] \\ (\boldsymbol{x}, t) & \mapsto d(\boldsymbol{x}, t) \end{cases} \tag{2.6}$$

in the solid $\mathcal{B}$. Then the crack functional becomes

$$\Gamma_l(d) := \int_{\mathcal{B}} \gamma(d; \nabla d) dV \tag{2.7}$$

with the crack density function

$$\gamma(d; \nabla d) = \frac{1}{c_0} \left(\frac{1}{l} \alpha(d) + l |\nabla d|^2 \right) . \tag{2.8}$$

The crack density function depending on the crack-phase-field and its spatial gradient represents the density of the crack surface per unit volume. Assume a sharp crack surface topology $\Gamma(t) \subset R^{\delta-1}$ inside the solid $\mathcal{B}$ at time t, as demonstrated in Figure 2.2. Then, from the minimization principle, the regularized crack phase-field $d(\boldsymbol{x}, t)$ is obtained over the crack phase-field localization zone $\mathcal{L}$

$$d = \text{Arg}\{ \inf_{d \in W_{\Gamma(t)}} \Gamma_l(d) \} \tag{2.9}$$

subjected to the Dirichlet boundary conditions

$$W_{\Gamma(t)} = \{ d | d(\boldsymbol{x}, t) = 1, \quad \text{at} \quad \boldsymbol{x} \in \Gamma(t) \} \tag{2.10}$$

The Euler equations of the above variational principle are

$$\alpha'(d) - 2l\Delta d(x) = 0 \quad \text{in} \quad \mathcal{B} \quad \text{and} \quad \nabla d \cdot \boldsymbol{n}_{\mathcal{L}} = 0 \quad \text{on} \quad \partial\mathcal{L} \tag{2.11}$$

where Δd is the Laplacian of the crack phase-field ($\Delta d := \mathrm{div}(\nabla d)$) and $\boldsymbol{n}_{\mathcal{L}}$ presents the outward unit normal on $\partial\mathcal{L}$.

2.3 Geometric Crack Function

In this section, the effect of the geometric crack function $\alpha(d)$ on the distribution of crack phase-field is examined. The crack phase-field function in (2.1) is not the unique one to regularize the crack topology. The crack surface density function $\gamma(d; \nabla d)$ depends on the geometric crack function governing the distribution of the crack phase-field and the value of the scaling parameter c_0. The geometric crack function $\alpha(d) \subset [0, 1]$ should satisfy

$$\alpha(0) = 0 \quad \text{and} \quad \alpha(1) = 1. \tag{2.12}$$

to fulfill the property phase-field $d \subset [0, 1]$.

One example of a geometric crack function from [67] is

$$\alpha(d) = \xi d + (1 - \xi)d^2 \in [0, 1] \quad \forall d \in [0, 1] \tag{2.13}$$

for $\xi \in [0, 2]$ and $\alpha \in [0, 1]$. Commonly used geometric crack functions and the resulting crack phase-fields $d(x)$ are summarized in Table 2.1 and their plots are given in Figures 2.3 and 2.4.

Table 2.1: Geometric crack functions $\alpha(d)$ and the corresponding crack phase-field functions $d(x)$

$\alpha(d)$	ξ	c_0	$d(x)$
d^2	0	2	$\exp\left(\frac{-\lvert x\rvert}{l}\right)$
d	1	8/3	$\left(1 - \frac{\lvert x\rvert}{2l}\right)^2$
$2d - d^2$	2	π	$1 - \sin\left(\frac{\lvert x\rvert}{l}\right)$

From Table 2.1 and Figure 2.4, it can be seen that the distribution of the crack phase-field depends on the geometric crack function.

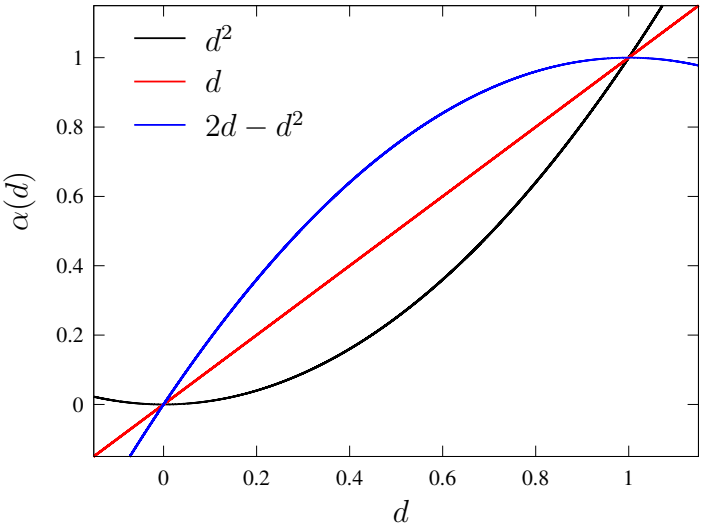

Figure 2.3: Geometric crack functions.

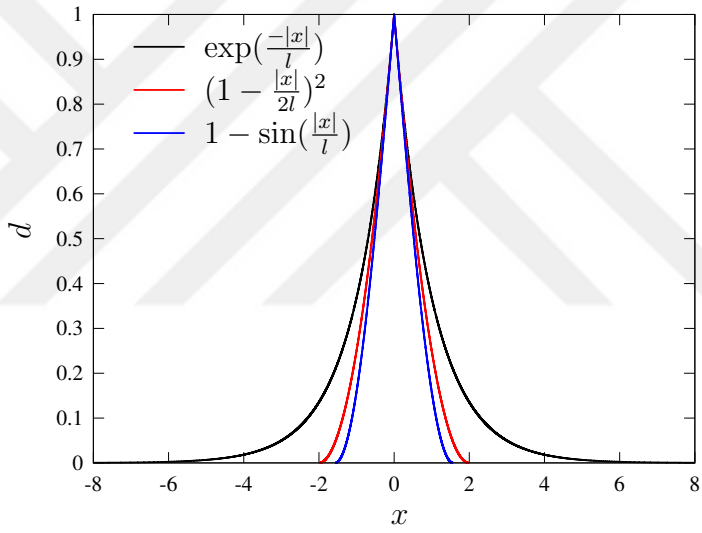

Figure 2.4: Phase-field profiles.

2.4 Energetic Degradation Function

As the crack grows, the initial free energy function Ψ_0 of the strain tensor $\boldsymbol{\varepsilon}$ is degraded by the energetic degradation function $g : d \to g(d) : [0, 1] \to [1, 0]$

$$\Psi(\boldsymbol{\varepsilon}, d) = g(d)\Psi_0(\boldsymbol{\varepsilon}) \tag{2.14}$$

where $g(0) = 1$ represents the intact state and $g(1) = 0$ represents fully broken state of the material. The energetic degradation function also satisfies that it is a mono-

tonically decreasing function and $g'(1) = 0$. The property $g'(1) = 0$ guarantees that the localization band does not grow orthogonally. Some of the degradation functions from the literature are given in Table 2.2 and their comparison by the phase-field variable is given in Figure 2.5.

Table 2.2: Degradation functions

$g(d)$	References
$(1-d)^2$	Bourdin et al. [68]
$(1-d)^2(2d+1)$	Kuhn et al. [69]
$(1-d)^3(3d+1)$	Kuhn et al. [69]
$\frac{e^{100d}-e^{100}(100d-99)}{99e^{100}+1}$	Steinke et al. [30]

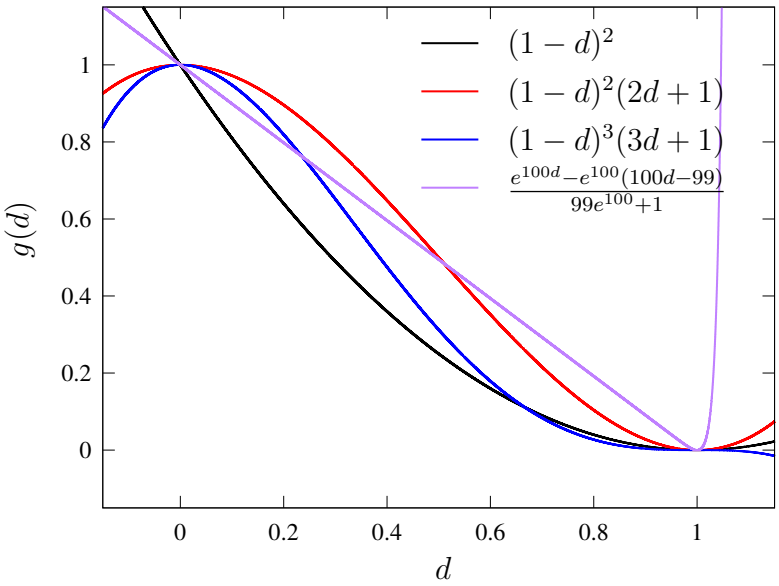

Figure 2.5: Example of degradation functions from literature.

2.5 Free Energy Function

The initial Helmholtz free energy function $\Psi_0(\boldsymbol{\varepsilon})$ for an isotropic solid is given by

$$\Psi_0(\boldsymbol{\varepsilon}) := \frac{\lambda}{2} \overset{2}{\mathrm{tr}}(\boldsymbol{\varepsilon}) + \mu \,\mathrm{tr}(\boldsymbol{\varepsilon}^2) \tag{2.15}$$

where the Lamé constant λ and the shear modulus μ can be written in terms of Elastic modulus E and Poisson's ratio ν as

$$\lambda = \frac{E\nu}{(1+\nu)(1-2\nu)}, \quad \mu = \frac{E}{2(1+\nu)} \tag{2.16}$$

2.6 Variational Equations and Governing Equations

In this section, a constitutive framework for the phase-field model of fracture is developed [70]. The state of a material point $\boldsymbol{x}$ at time t is defined by the displacement field $\boldsymbol{u}(\boldsymbol{x}, t)$ and $d(\boldsymbol{x}, t)$

$$\text{State}(\boldsymbol{x}, t) := \{\boldsymbol{\varepsilon}(\boldsymbol{x}, t), d(\boldsymbol{x}, t)\} \tag{2.17}$$

The displacement field $\boldsymbol{u}(\boldsymbol{x}, t)$ of the material point $\boldsymbol{x} \in \mathcal{B}$ at time $t \in \mathcal{T}$ is defined as

$$\boldsymbol{u} : \begin{cases} \mathcal{B} \times \mathcal{T} & \to R^{\delta} \\ (\boldsymbol{x}, t) & \mapsto \boldsymbol{u}(\boldsymbol{x}, t) \end{cases} \tag{2.18}$$

As a result, the strain tensor is given as

$$\boldsymbol{\varepsilon}(\boldsymbol{u}) := \nabla^{sym}\boldsymbol{u} = \frac{1}{2}[\nabla^T \boldsymbol{u} + \nabla \boldsymbol{u}] \tag{2.19}$$

Then, the constitutive free energy functional is defined by

$$\mathcal{E}(\boldsymbol{u}, d) := \int_{\mathcal{B}} \Psi(\boldsymbol{\varepsilon}(\boldsymbol{u}), d) dV \tag{2.20}$$

The equations for macro and micro balance are obtained by using the principle of virtual work

$$\dot{\mathcal{E}}(\boldsymbol{u}, d, \dot{\boldsymbol{u}}, \dot{d}) + \mathcal{D}(\dot{d}, d) - \mathcal{P}(\dot{\boldsymbol{u}}) = 0 \tag{2.21}$$

where $\dot{\mathcal{E}}$ is the rate of the energy storage functional, $\mathcal{P}(\dot{\boldsymbol{u}})$ is the external power functional and $\mathcal{D}$ is the dissipation functional.

They are defined as

$$\begin{aligned} \dot{\mathcal{E}}(\dot{\boldsymbol{u}}, \dot{d}) &:= \int_{\mathcal{B}} [\partial_d \Psi \dot{d} + \partial_{\boldsymbol{\varepsilon}} \Psi : \dot{\boldsymbol{\varepsilon}}] \, dV \\ \mathcal{P}(\dot{\boldsymbol{u}}) &:= \int_{\mathcal{B}} \bar{\boldsymbol{b}}(\boldsymbol{x}, t) \cdot \dot{\boldsymbol{u}} \, dV + \int_{\partial \mathcal{B}_t} \bar{\boldsymbol{t}}(\boldsymbol{x}, t) \cdot \dot{\boldsymbol{u}} \, dA \\ \mathcal{D}(\dot{d}, d) &:= \int_{\mathcal{L}} \Phi(d, \nabla d, \dot{d}, \nabla \dot{d}) \, dV \end{aligned} \tag{2.22}$$

where $\Phi(d, \nabla d, \dot{d}, \nabla \dot{d})$ is the constitutive dissipation function per unit volume, $\bar{\boldsymbol{b}}$ is the body force, and $\bar{\boldsymbol{t}}$ is the traction.

Insertion of (2.22) into (2.21) and application of the Gauss integral theorem yields

$$\begin{aligned} &\int_{\mathcal{B}} \left[-[\operatorname{div}(\boldsymbol{\sigma}) + \bar{\boldsymbol{b}}] \cdot \dot{\boldsymbol{u}} + [\partial_d \Psi - \operatorname{div}(\partial_{\nabla d} \dot{\Phi})] \dot{d} \right] dV \\ &+ \int_{\partial \mathcal{B}_t} [\boldsymbol{\sigma} \cdot \boldsymbol{n} - \bar{\boldsymbol{t}}] \cdot \dot{\boldsymbol{u}} dA + \int_{\partial \mathcal{L}} [\partial_{\nabla d} \Psi \cdot \boldsymbol{n}] \dot{d} dA = 0 \end{aligned} \tag{2.23}$$

where

$$\boldsymbol{\sigma} = \partial_{\boldsymbol{\varepsilon}} \Psi. \tag{2.24}$$

From (2.23) the two coupled balance equations are obtained

$$\begin{aligned} \operatorname{div}(\boldsymbol{\sigma}) + \bar{\boldsymbol{b}} &= \boldsymbol{0} \\ \operatorname{div}(\partial_{\nabla d} \Phi) - [\partial_d \Psi] &= 0 \end{aligned} \tag{2.25}$$

with the Neumann-type boundary conditions

$$\boldsymbol{\sigma n} = \bar{\boldsymbol{t}} \quad \text{on} \quad \partial\mathcal{B}_t \quad \text{and} \quad \partial_{\nabla d}\Phi \cdot \boldsymbol{n} = 0 \quad \text{on} \quad \partial\mathcal{L}\,. \tag{2.26}$$

2.7 1-D Analytical Solution

Let a bar with a domain of $x \in [-L, L]$ be loaded at both ends by the displacement u along opposite outward directions [71]. Under these conditions and in the absence of body forces, the following balance and constitutive equations hold.

$$\sigma_{,x} = 0 \tag{2.27}$$

$$\frac{g_c}{l}[\frac{1}{l}\alpha'(d) - 2l d_{,xx}] + \frac{1}{2}g'(d)E_0\varepsilon^2 = 0 \tag{2.28}$$

$$\sigma = g(d)E_0\varepsilon \tag{2.29}$$

where the first expression (2.43) is the linear momentum equation in the absence of body forces, the second equation (2.28) is the evolution equation of the phase-field d, and the third equation (2.29) is the constitutive relation between stress and strain. The linear elastic stress-strain relation is assumed in the intact state with $(d = 0)$.

Let us introduce a function $w(d)$ in terms of $g(d)$ such that

$$w(d) := \frac{1}{g(d)} - 1\,. \tag{2.30}$$

Then, the evolution equation and the constitutive equation yields

$$\sigma^2 w'(d) - A_0[\alpha'(d) - 2l^2 d_{,xx}] = 0 \quad \text{and} \quad A_0 := \frac{2E_0 g_c}{c_0 l}\,. \tag{2.31}$$

2.7.1 Homogenous Solution

For the homogenous solution, the crack phase-field is uniform along the bar i.e. $d_{,xx} = 0$. Then Equation (2.31) becomes

$$\sigma^2 w'(d) - A_0 \alpha'(d) = 0 \tag{2.32}$$

which yields

$$\sigma = \sqrt{A_0 \frac{\alpha'(d)}{w'(d)}} \quad \text{and} \quad \varepsilon = \frac{1}{E_0}\sqrt{-A_0 \frac{\alpha'(d)}{g'(d)}} \tag{2.33}$$

Let $\sigma(d)$ reaches its peak value at d_c. Then the critical stress σ_c and the corresponding strain ε_c are defined as

$$\sigma_c = \sigma(d_c) \quad \text{and} \quad \varepsilon_c = \varepsilon(d_c) \tag{2.34}$$

2.7.2 Localized Solution

The homogenous solution is only applicable when $\varepsilon < \varepsilon_c$. When $\varepsilon > \varepsilon_c$, the crack phase-field localizes into a localization band and $d_{,xx}$ is can no longer be assumed to be 0. Assume that the crack is initiated at $x = 0$ and localized in the region where $x \in [-D, D]$ with half bandwidth D is sufficiently smaller than L. The boundary conditions of the above setting yield $w(d = 0) = 0$. Multiplying Equation (2.31) with $d_{,x}$ and integrating it over the localization band with respect to x considering the above condition yields

$$\sigma^2 w(d) - A_0[\alpha'(d) - l^2 d_{,x}^2] = 0 \quad \text{with} \quad A_0 = \frac{2E_0 g_c}{c_0 l}\,. \tag{2.35}$$

At $x = 0$, the crack phase-field has its maximum value d_* and at that point, $d_{,x} = 0$. The stress at this point then becomes

$$\sigma(d_*) = \sqrt{A_0 \frac{\alpha'(d_*)}{g'(d_*)}}\,. \tag{2.36}$$

Equations (2.35) and (2.36) yield

$$d_{,x}^2 = \frac{1}{l^2}[\alpha(d) - \frac{\alpha(d_*)w(d)}{w(d_*)}]\,. \tag{2.37}$$

For $x \geq 0$, since the crack phase-field $d(x)$ is a monotonically decreasing function, its derivative $d_{,x} \leq 0$. Therefore, the derivative of the crack phase-field becomes

$$d_{,x} = -\frac{1}{l}\mathcal{F} \quad \text{with} \quad \mathcal{F}(d; d_*) = \sqrt{\alpha(d) - \frac{\alpha(d_*)w(d)}{w(d_*)}}\,. \tag{2.38}$$

2.7.3 Particular Examples

In this section, the above results are applied to the examples with the quadratic geometric crack function $\alpha(d) = d^2$ and the degradation function $g(d) = (1-d)^2$. For the quadratic geometric crack function $\alpha(d) = d^2$ the following properties hold

$$\xi = 0 \quad \text{and} \quad c_0 = 2 \tag{2.39}$$

Furthermore, for this case, the critical phase-field d_c is obtained from

$$\frac{\partial \sigma}{\partial d} = 0, \quad d \in [0, 1] \tag{2.40}$$

2.7.3.1 Strain criterion without threshold

Following Equation (2.40), the critical phase-field d_c is solved as

$$d_c = \frac{1}{4} \tag{2.41}$$

and Equation (2.34) results in

$$\sigma_c = \frac{3}{16}\sqrt{\frac{3E_0 g_c}{l}} \quad \text{and} \quad \varepsilon_c = \sqrt{\frac{g_c}{3E_0 l}} \tag{2.42}$$

The stress response given from Equation (2.33) then becomes

$$\sigma = \left(\frac{g_c}{g_c + lE\varepsilon^2}\right)^2 E\varepsilon \tag{2.43}$$

2.7.3.2 Strain criterion with threshold

In this case, the balance and constitutive equations become

$$\sigma_{,x} = 0 \tag{2.44}$$

$$\Psi_c d - \Psi_c l^2 d_{,xx} - (1-d)\max_{s\in[0,t]}\langle \Psi_0(\varepsilon(x,s)) - \Psi_c\rangle_+ = 0 \tag{2.45}$$

where

$$\sigma = (1-d)^2 E_0 \varepsilon \tag{2.46}$$

and Ψ_c is the specific fracture energy per unit volume [26].

In the homogeneous case when $\Psi_0 < \Psi_c$, (2.45) reduces to

$$d = 0 \tag{2.47}$$

and from (2.46) the stress response is given as

$$\sigma = E\varepsilon \tag{2.48}$$

However, when $\Psi > \Psi_c$, (2.45) becomes

$$d = 1 - \frac{\Psi_c}{\Psi} \tag{2.49}$$

and from (2.46) the stress response is given as

$$\sigma = \frac{4\Psi_c^2}{E\varepsilon^3} \tag{2.50}$$

The critical strain value can be calculated from $\Psi(\varepsilon_c) = \Psi_c$ i.e.

$$\varepsilon_c = \sqrt{\frac{2\Psi_c}{E}} \tag{2.51}$$

Then, from (2.48) or (2.50), the critical stress value becomes

$$\sigma_c = \sqrt{2E\Psi_c} \tag{2.52}$$

Unlike (2.42) and (2.43), (2.50) and (2.52) do not depend on the length scale l.

2.8 Specific equations of the model

At this point, we provide the specific model equations corresponding to the geometric crack function $\alpha(d)$, the degradation function $g(d)$, and the dissipation function $\phi(d)$ of the crack phase-field d described previously. Let the geometric crack function [67] be

$$\alpha(d) = d^2 \tag{2.53}$$

and the degradation function [68] be

$$g(d) = (1-d)^2 \tag{2.54}$$

2.8.1 Strain criterion without threshold

In the strain criteria without threshold [26], the constitutive dissipation function is defined as

$$\Phi(d, \nabla d, \dot{d}, \nabla \dot{d}) = \left(\frac{g_c}{l} d\right) \dot{d} + (g_c l \nabla d) \cdot \nabla \dot{d}\,. \tag{2.55}$$

Then the second equation of (2.25) becomes

$$\frac{g_c}{l}[d - l^2\Delta d] - [2(1-d)\mathcal{H}(\boldsymbol{x},t)] = 0 \tag{2.56}$$

where $\mathcal{H}(\boldsymbol{x},t)$ is the local history field of the maximum free energy function and for the strain criterion without threshold, it is defined as

$$\mathcal{H}(\boldsymbol{x},t) := \max_{s\in[0,t]} \Psi_0(\boldsymbol{\varepsilon}(\boldsymbol{x},s)) \tag{2.57}$$

2.8.2 Strain criterion with threshold

In the strain criterion with threshold [26], the constitutive dissipation function is defined as

$$\Phi(d, \nabla d, \dot{d}, \nabla\dot{d}) = 2\Psi_c(\dot{d} + \frac{l^2}{2}\nabla d\nabla\dot{d}) \tag{2.58}$$

Then the second equation of (2.25) becomes

$$2\Psi_c[d - l^2\Delta d] - [2(1-d)\mathcal{H}(\boldsymbol{x},t)] = 0 \tag{2.59}$$

The local history field of maximum dissipation function for strain criterion with threshold is defined as

$$\mathcal{H}(\boldsymbol{x},t) := \max_{s\in[0,t]} \zeta\langle\Psi_0(\boldsymbol{\varepsilon}(\boldsymbol{x},s)) - \Psi_c\rangle_+ \tag{2.60}$$

where the additional dimensionles parameter ζ is the driving force slope [26].

In this study, the strain criterion with threshold (2.59) is employed for the numerical examples. The material parameters used in numerical examples along with the equations where they appear are given in Table 2.3.

Table 2.3: Material parameters used in the numerical examples

Parameter	Description	Unit	Equation
Ψ_c	Critical fracture energy	kJ/m^3	(2.59)
E	Elastic modulus	GPa	(2.16)
ν	Poisson's ratio	-	(2.16)
ζ	Driving force slope	-	(2.60)

2.8.3 Hybrid Formulation

In this study we use the so-called hybrid formulation (Ambati et al. [28]) where the evolution of the phase-field d is driven by the tensile part of free energy Ψ_0^+ to avoid cracking in compression. However, the free energy for the stress response (2.24) remains isotropic to keep the computational cost comparable to that of the isotropic model. Ψ_0^+ is defined as

$$\Psi_0^+(\boldsymbol{\varepsilon}) := \frac{\lambda}{2}\langle \mathrm{tr}(\boldsymbol{\varepsilon})\rangle_+^2 + \mu\,\mathrm{tr}(\boldsymbol{\varepsilon}_+^2) \quad \text{with} \quad \boldsymbol{\varepsilon}_+ := \Sigma_i^3 \langle \varepsilon_i \rangle_+ \boldsymbol{n}_i \otimes \boldsymbol{n}_i \tag{2.61}$$

where ε_i and $\boldsymbol{n}_i$ ($i \in \{1,2,3\}$) are eigenvalues and eigenvectors of the strain tensor $\boldsymbol{\varepsilon}$.

CHAPTER 3

FINITE ELEMENT FORMULATION

In this chapter, we explore the application of the conventional Galerkin method to obtain the weak form of the conservation of linear momentum and the evolution equation for the crack phase-field. To achieve this, we utilize square-integrable weight functions that satisfy the homogeneous Dirichlet-type boundary conditions ($\delta u = 0$ on $\partial\mathcal{B}_u$ and $\delta d = 0$ on $\partial\mathcal{L}_d$). These weight functions are multiplied with the local residual differential equations given in (2.25). By integrating the resulting weighted residual equations over the domain using integration by parts, we derive the weighted residual expressions governing the balance of linear momentum.

$$G^u(\delta\boldsymbol{u};\boldsymbol{u},d) = G^u_{int}(\delta\boldsymbol{u};\boldsymbol{u},d) - G^u_{ext}(\delta\boldsymbol{u}) = 0 \tag{3.1}$$

and the evolution of the phase-field

$$G^d(\delta d;\boldsymbol{u},d) = G^d_{int}(\delta d;\boldsymbol{u},d) - G^d_{ext}(\delta d;\boldsymbol{u},d) = 0\,. \tag{3.2}$$

The terms G^u_{int} and G^u_{ext} are defined as

$$\begin{aligned} G^u_{int}(\delta\boldsymbol{u};\boldsymbol{u},d) &:= \int_{\mathcal{B}} \delta\boldsymbol{\varepsilon} : \boldsymbol{\sigma}\, dV, \\ G^u_{ext}(\delta\boldsymbol{u}) &:= \int_{\mathcal{B}} \delta\boldsymbol{u}\cdot\bar{\boldsymbol{b}}\, dV + \int_{\partial\mathcal{B}_t} \delta\boldsymbol{u}\cdot\bar{\boldsymbol{t}}\, dA \end{aligned} \tag{3.3}$$

and the terms G^d_{int} and G^d_{ext} are given by

$$\begin{aligned} G^d_{int}(\delta d;\boldsymbol{u},d) &:= \int_{\mathcal{B}} \nabla(\delta d)\cdot(\Psi_c l^2\nabla d)\, dV, \\ G^d_{ext}(\delta d;\boldsymbol{u},d) &:= \int_{\mathcal{B}} \delta d((1-d)\mathcal{H} - \Psi_c d)\, dV. \end{aligned} \tag{3.4}$$

Now, we discretize the entire domain $\mathcal{B}$ into finite elements with a volume of $\mathcal{B}_e^h$. Within each element domain of $\mathcal{B}_e^h$, we utilize finite element interpolations to estimate the displacement $\boldsymbol{u}$ and the phase-field d, along with their virtual counterparts $\delta\boldsymbol{u}$ and δd

$$\boldsymbol{u}_e^h = \sum_{i=1}^{n_{en}} \boldsymbol{N}_i^u \boldsymbol{U}_i^e \,, \quad d_e^h = \sum_{i=1}^{n_{en}} N_i^d D_i^e \,, \tag{3.5}$$

$$\delta\boldsymbol{u}_e^h = \sum_{i=1}^{n_{en}} \boldsymbol{N}_i^u \delta\boldsymbol{U}_i^e \,, \quad \delta d_e^h = \sum_{i=1}^{n_{en}} N_i^d \delta D_i^e \,, \tag{3.6}$$

where n_{en} represents the number of nodes within each element. In the given context, D_i^e represents the phase-field variable associated with a specific Node i within the element, while N_i^d represents its shape function. Moreover, $\boldsymbol{U}_i^e$ and $\delta\boldsymbol{U}_i^e$ are the vectors of the displacements and their virtual counterparts, and $\boldsymbol{N}_i^u$ is the associated matrix of shape functions linked to Node i. In the case of a two-dimensional problem, these expressions are formulated as follows:

$$\boldsymbol{U}_i^e = \begin{bmatrix} u_1^e \\ u_2^e \end{bmatrix} \,, \quad \delta\boldsymbol{U}_i^e = \begin{bmatrix} \delta u_1^e \\ \delta u_2^e \end{bmatrix} \,, \quad \boldsymbol{N}_i^u = \begin{bmatrix} N_i^u & 0 \\ 0 & N_i^u \end{bmatrix} \tag{3.7}$$

The strain tensor $\boldsymbol{\varepsilon}$ and the gradient of the phase-field ∇d as well as their virtual counterparts $\delta\boldsymbol{\varepsilon}$ and $\nabla(\delta d)$ are approximated by

$$\boldsymbol{\varepsilon}_e^h = \sum_{i=1}^{n_{en}} \boldsymbol{B}_i^u \boldsymbol{U}_i^e \,, \quad \nabla d_e^h = \sum_{i=1}^{n_{en}} \boldsymbol{B}_i^d D_i^e \tag{3.8}$$

$$\delta\boldsymbol{\varepsilon}_e^h = \sum_{i=1}^{n_{en}} \boldsymbol{B}_i^u \delta\boldsymbol{U}_i^e \,, \quad \nabla(\delta d)_e^h = \sum_{i=1}^{n_{en}} \boldsymbol{B}_i^d \delta D_i^e \tag{3.9}$$

where $\boldsymbol{B}_i^u$ and $\boldsymbol{B}_i^d$ are matrices of derivatives of shape functions correspond to Node i. In the two-dimensional setting, they are defined as

$$\boldsymbol{B}_i^u = \begin{bmatrix} \frac{\partial N_i^u}{\partial x_1} & 0 \\ 0 & \frac{\partial N_i^u}{\partial x_2} \\ \frac{\partial N_i^u}{\partial x_2} & \frac{\partial N_i^u}{\partial x_1} \end{bmatrix} \,, \quad \boldsymbol{B}_i^d = \begin{bmatrix} \frac{\partial N_i^d}{\partial x_1} \\ \frac{\partial N_i^d}{\partial x_2} \end{bmatrix} \tag{3.10}$$

Substitution of the finite element discretizations (3.5), (3.6), (3.8), and (3.9) into the weak forms (3.1) and (3.2) and assembling over the elements leads to the following system of linearized equations:

$$\begin{bmatrix} \tilde{\boldsymbol{R}}^u \\ \tilde{\boldsymbol{R}}^d \end{bmatrix} + \begin{bmatrix} \tilde{\boldsymbol{K}}^{uu} & \tilde{\boldsymbol{K}}^{ud} \\ \tilde{\boldsymbol{K}}^{du} & \tilde{\boldsymbol{K}}^{dd} \end{bmatrix} \begin{bmatrix} \Delta \boldsymbol{U} \\ \Delta \boldsymbol{D} \end{bmatrix} = \begin{bmatrix} \mathbf{0} \\ \mathbf{0} \end{bmatrix} . \tag{3.11}$$

The system involves evaluating the difference between two sets of variables $\Delta \boldsymbol{U}$, which is the difference between the global displacement vector $\boldsymbol{U}$ and its counterpart at previous iteration $\tilde{\boldsymbol{U}}$, and $\Delta \boldsymbol{D}$, which is the difference between global phase-field vector $\boldsymbol{D}$ and its counterpart at the previous iteration $\tilde{\boldsymbol{D}}$. The global residual vectors $\tilde{\boldsymbol{R}}^u$ and $\tilde{\boldsymbol{R}}^d$, and the global stiffness matrices $\tilde{\boldsymbol{K}}^{uu}$, $\tilde{\boldsymbol{K}}^{ud}$, $\tilde{\boldsymbol{K}}^{du}$, and $\tilde{\boldsymbol{K}}^{dd}$ are evaluated at previous iterations $\tilde{\boldsymbol{U}}$ and $\tilde{\boldsymbol{D}}$.

The global residual vectors and stiffness matrices are computed by the sum of local values at element nodes where the assembly operator combines the contributions of local values at nodes $i, j, k, l = 1, ..., n_{en}$ and assigns them to their corresponding global counterparts at nodes $I, J, K, L = 1, ..., n_{nd}$ in the finite element mesh with n_{nd} being the total number of nodes in the mesh.

To solve the system of iterative finite element equations (3.11), a staggered scheme that decreases the size of the problem consequently and computational cost significantly can be used:

$$\boldsymbol{R}^u + \boldsymbol{K}^{uu} \Delta \boldsymbol{U} = \boldsymbol{0} \tag{3.12}$$

$$\boldsymbol{R}^d + \boldsymbol{K}^{dd} \Delta \boldsymbol{D} = \boldsymbol{0} \tag{3.13}$$

So, the solution for the displacement field and phase-field is obtained through the successive solution of the above equations. The algorithm for the staggered scheme is given in Box 1.

Box 1: Algorithm for the staggered scheme.

For given nodal phase-field variables $\boldsymbol{D}_n$, and nodal displacements $\boldsymbol{U}_n$ at time t_n:

- Compute current displacements $\boldsymbol{U}_{n+1}$ by

$$\int_{\mathcal{B}} \left[\boldsymbol{B}_u^T \boldsymbol{\sigma}(\boldsymbol{\varepsilon}, d_n) - \boldsymbol{N}_u^T \bar{\boldsymbol{b}}\right] dV - \int_{\partial \mathcal{B}_t} \boldsymbol{N}_u^T \bar{\boldsymbol{t}}\, dA. \tag{3.14}$$

- Compute current phase-field variables $\boldsymbol{D}_{n+1}$ by

$$\int_{\mathcal{B}} \left[\Psi_c l^2 \boldsymbol{B}_d^T \nabla d - \boldsymbol{N}_d^T((1-d)\mathcal{H}_n - \Psi_c d))\right] dV. \tag{3.15}$$

- Update $\boldsymbol{U}_{n+1}$, and $\boldsymbol{D}_{n+1}$ at time t_{n+1}.

CHAPTER 4

NUMERICAL EXAMPLES

This section showcases the modeling capabilities of phase-field modeling in relation to brittle fracture through various numerical examples. The phase-field modeling approach is employed to simulate the brittle fracture in layered solids particularly additively manufactured concrete and masonry walls under mechanical loading using several specimens and loading types using the scientific computing program FEniCS Project [72]. The results generated by FEniCS have been post-processed by the scientific visualization program ParaView [73].

4.1 Validations

In this section, the examples to validate the numerical model are presented. These examples include the mesh objectivity of the model, the length scale independence of the model, and the comparison of the numerical model with experimental data.

4.1.1 Mesh objectivity of the model

To ensure accurate numerical results for fracture under mechanical loading, a convergence study on mesh dependence is conducted on tension test of a single-edge notched plate. The plate is restrained on the bottom edge horizontally and vertically. The plate's geometry and dimensions are illustrated in Figure 4.1.

A mesh composed of three-node triangular elements is used to discretize the domain and in each analysis, different mesh sizes are employed to investigate the effect of the mesh size on the results of the analysis. The length scale is kept constant at $l = 0.8$

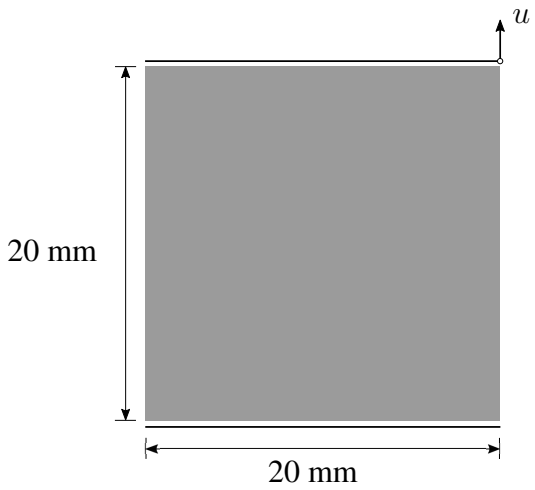

Figure 4.1: Geometry, dimensions, and boundary conditions for tension test.

Table 4.1: Material parameters used in the mesh convergence example

Parameter	Description	Unit	Value
Ψ_c	Critical fracture energy	kJ/m^3	10
E	Elastic modulus	GPa	2.4
ν	Poisson's ratio	-	0.2
ζ	Driving force slope	-	15

mm, and the element size of the mesh with the lowest number of elements is set to $h = l/2$ to provide sufficiently correct regularization of the crack surface functional Γ_l. The values of the material parameters of the specimen are provided in Table 4.1.

The loading in which the displacement is controlled is simulated by gradually increasing the displacement on the top surface of the specimen. In the first 80 steps, the displacement increment is set to 1×10^{-4} mm, while in the following time steps, it is reduced to 1×10^{-6} mm to be able to observe the brittle nature of crack propagation. To evaluate the structural response of a brittle phase-field model for fracturing material, load-displacement curves are plotted in Figure 4.2 for various element sizes. It is

observed that the structural response does not depend on the element size, as refining the mesh to a sufficient extent, the convergence of the results is observed.

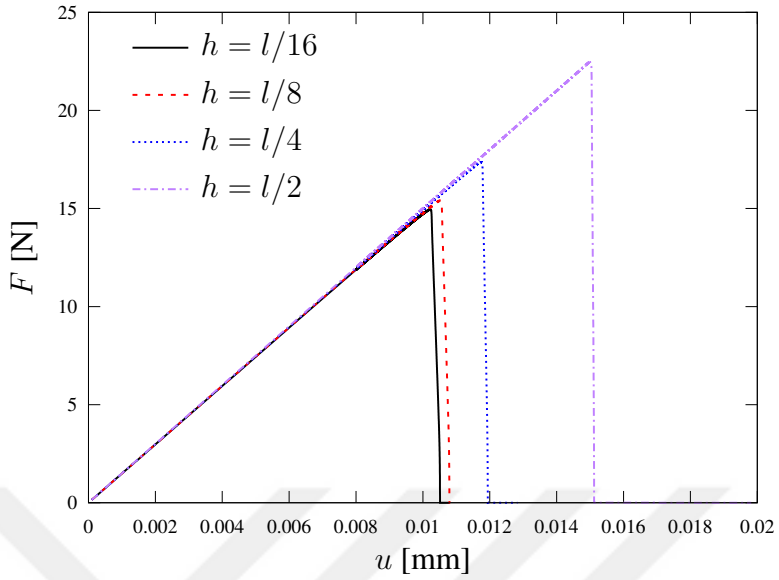

Figure 4.2: Load-displacement curves for each mesh size of the mesh objectivity study.

4.1.2 Length-scale independence of the model

In this study, the strain criterion with threshold (2.59) is employed for the numerical examples. Since this energetic criterion is independent of the length scale l, we do not need to treat l as a material parameter. To test this feature, a study on length-scale independence is conducted on a three-point bending test. The beam's geometry and dimensions are illustrated in Figure 4.3.

A mesh consisting of three-node triangular elements is used to discretize the domain. The mesh is refined in the middle region of the beam where cracking is expected as shown in Figure 4.4. The element size is kept constant at $h = 0.1$ mm, and the length scale of the analysis with the smallest length scale is set to $h = l/2$ to provide sufficiently correct regularization of the crack surface functional Γ_l. The material parameters of the beam are provided in Table 4.2.

The loading in which the displacement is controlled is simulated by gradually in-

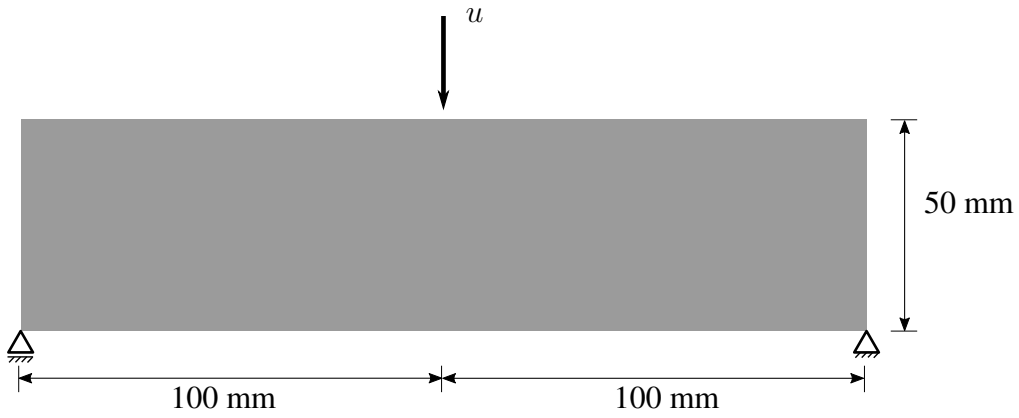

Figure 4.3: Three-point bending test. Geometry, and boundary conditions for length-scale independence and experimental validation examples.

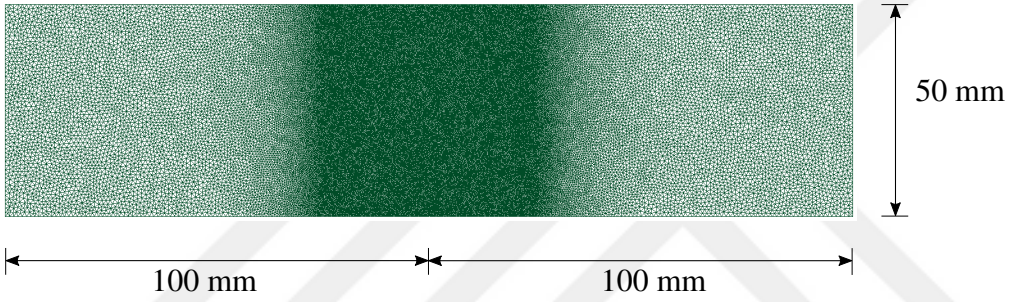

Figure 4.4: Finite element mesh for the beam used in length-scale independence and experimental validation examples.

Table 4.2: Material parameters used in the length scale independence example

Parameter	Description	Unit	Value
Ψ_c	Critical fracture energy	kJ/m^3	6
E	Elastic modulus	GPa	2.4
ν	Poisson's ratio	-	0.2
ζ	Driving force slope	-	15

creasing the displacement at the center of the top surface of the specimen. The displacement increment is set to 1×10^{-4} mm. To evaluate the structural response of the brittle phase-field model for fracturing material, load-displacement curves are plotted in Figure 4.5 for various length scales. It is observed that the structural response does not depend on the length scale as the curves for each length scale almost coincide.

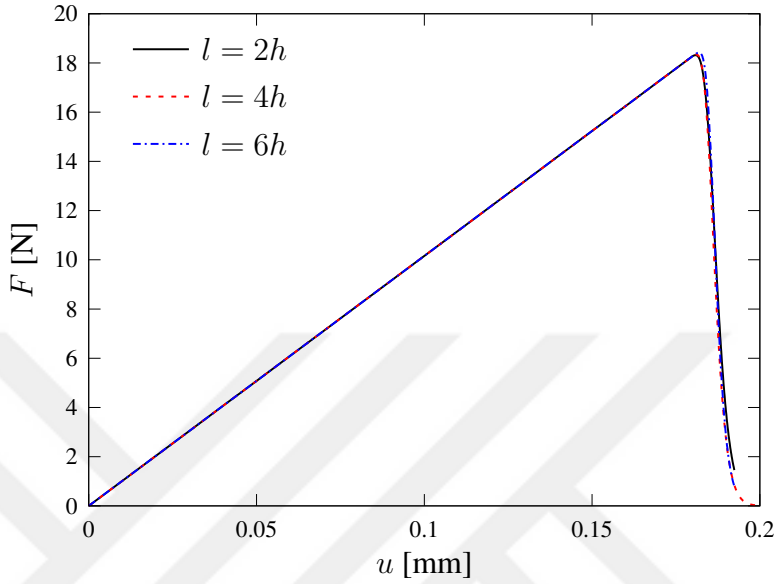

Figure 4.5: Load-displacement curves for different values of the length scales.

4.1.3 Experimental Validation

In this example, we compare the current work with experimental data. The experiment is a three-point bending test of an additively manufactured plain concrete beam from Ma et al. [60]. The geometry, boundary conditions, and loading are shown in Figure 4.3, and the mesh is finely refined with an effective element size of 0.1 mm in the central strip where the crack is expected to propagate as shown in Figure 4.4. The beam is composed of 10 layers and we choose the interface thickness as 0.4 mm. The material parameters are given in Table 4.3. The interface thickness and the material parameters are selected based on the studies [49, 54, 60, 62–64].

Displacement-driven loading is simulated by gradually increasing the displacement with an increment of 1×10^{-4} mm. The increment size is selected as small as that; making it smaller does not change the global load-displacement response. The crack

Table 4.3: Material parameters for the layered specimens

Parameter	Description	Unit	Value
Ψ_c^l	Critical fracture energy for layers	kJ/m^3	10
Ψ_c^i	Critical fracture energy for interfaces	kJ/m^3	2
E	Elastic modulus	GPa	2.4
ν	Poisson's ratio	-	0.2
ζ	Driving force slope	-	15

pattern predicted by the model is given in Figure 4.6.

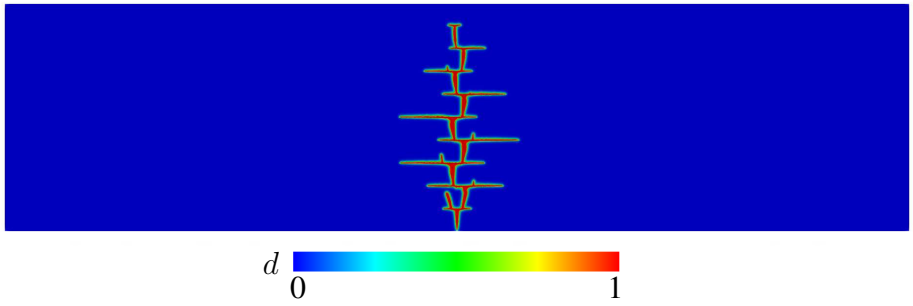

Figure 4.6: Experimental validation study. Crack pattern predicted by the model.

The load-displacement curves from the numerical model along with the experimental test are given in Figure 4.7. The numerical model captures the ultimate load, displacement and brittle behavior of the specimen.

The crack propagation patterns at different stages of the loading are given in Figure 4.8 where the labels of the stages correspond to the ones in Figure 4.7. The crack begins to localize at the bottom-middle of the specimen and propagates upwards with a "step-like" pattern.

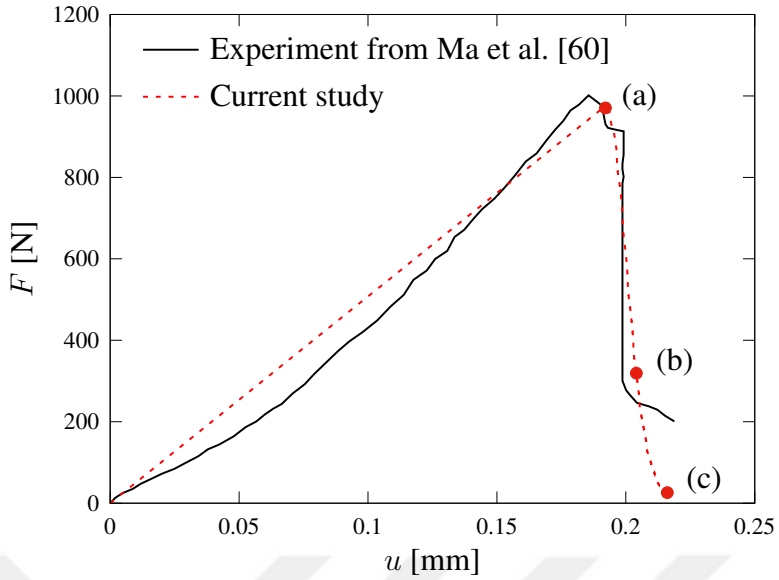

Figure 4.7: Experimental validation study. Comparison of experimental, and numerical load-displacement curves for additively manufactured concrete.

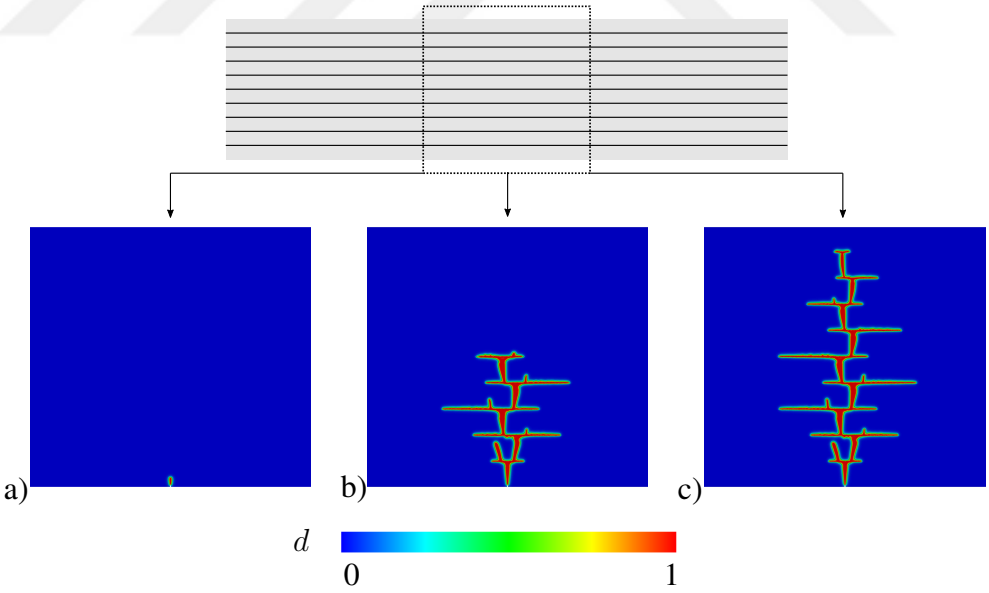

Figure 4.8: Experimental validation study. Crack propogation at a load of (a) $F = 970.60$ N, (b) $F = 319.31$ N, (c) $F \approx 0$ N, see Figure 4.7.

4.2 Application of the Model to Variety of Examples

Now, the validated model in the previous sections will be applied to various types of examples to investigate the mechanical performance of additively manufactured concrete. Because of the nature of the additive manufacturing process, additively manufactured concrete possesses a layered structure and the interfaces between the layers are weaker than the layers themselves. To address this issue, we consider different types of interfaces namely horizontal, triangular, and sinusoidal as shown in Figure 4.9 using four layers of concrete that are separated by interfaces. The triangular and sinusoidal interfaces have a height of 2.5 mm and a wavelength of 5 mm. In the following sections, we will investigate the effects of these interfaces on the mechanical performance and toughness of the additively manufactured concrete specimens subjected to various loading and boundary conditions.

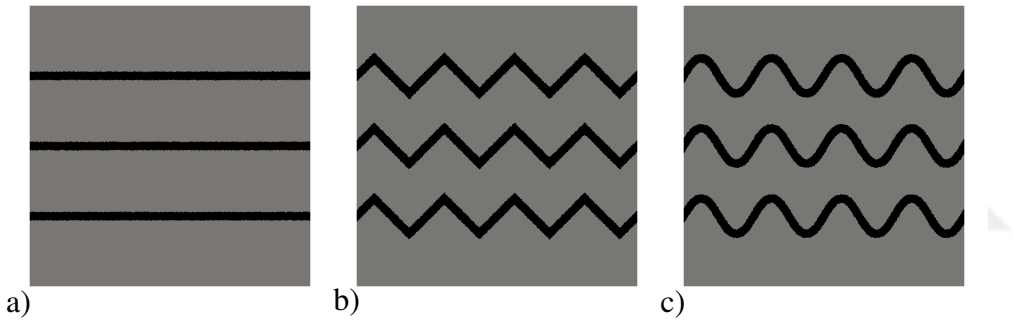

Figure 4.9: Interface types. (a) Horizontal, (b) triangular, and (c) sinusoidal interfaces. Interfaces are shown in black, and layers in gray.

4.2.1 Tension Test

In this example, a notch-less square plate with various layer configurations presented in Figure 4.9 is investigated under tension. The plate is restrained on the bottom surface horizontally and vertically. The geometry, boundary conditions, and loading are shown in Figure 4.1. The domain is divided into three-node triangular elements, with a size of $h = 0.1$ mm and the length scale is set to $l = 0.2$ mm. The specimen is composed of 4 layers and we choose the interface thickness as 0.6 mm. The material

parameters are given in Table 4.3.

Displacement-controlled loading is achieved by constantly increasing the displacement on the top surface with an increment of $\Delta u = 1 \times 10^{-5}$ mm. The phase-field profiles corresponding to the fully broken state of the specimen are given in Figure 4.10. The main crack occurs at the middle interface and also local cracks occur at the other interfaces of the specimen for all the interface types.

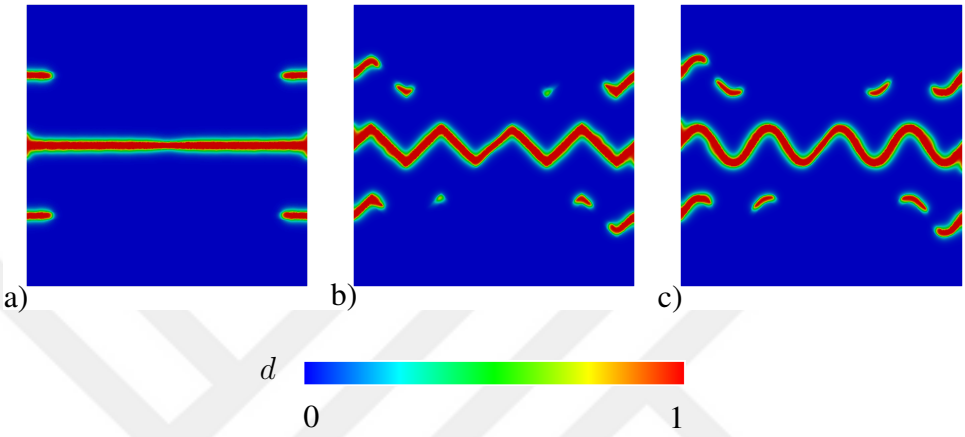

Figure 4.10: Tension test. Crack pattern for (a) horizontal, (b) triangular, and (c) sinusoidal interface types.

To evaluate the effect of the interface types on mechanical performance for the tension test, load-displacement curves for the different types of interface are plotted in Figure 4.11. It is observed that the interface types have no effect on mechanical performance under tension perpendicular to the layers.

For the specimen with the sinusoidal interface, the crack propagation patterns at different stages of the loading are given in Figure 4.12 where the labeling follows from the one used in Figure 4.11. The crack begins to localize at the center of the specimen and propagates toward both sides of the specimen.

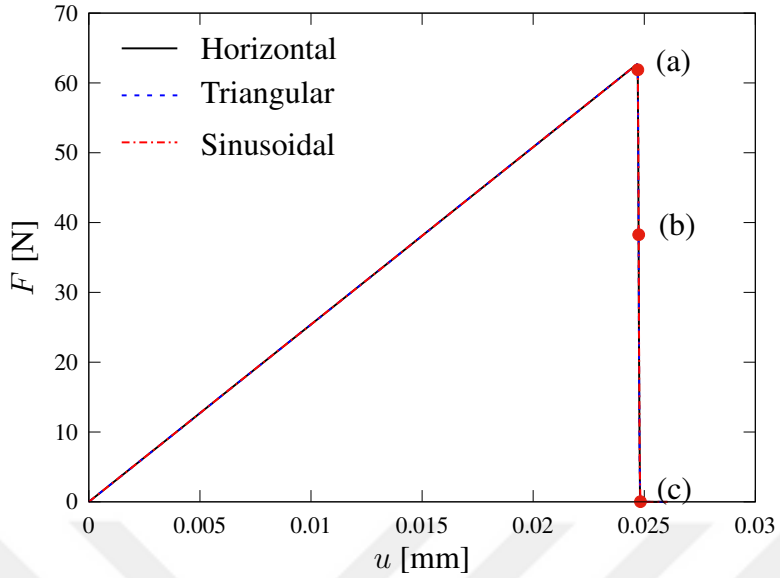

Figure 4.11: Tension test. Load-displacement curves for horizontal, triangular, and sinusoidal interface types.

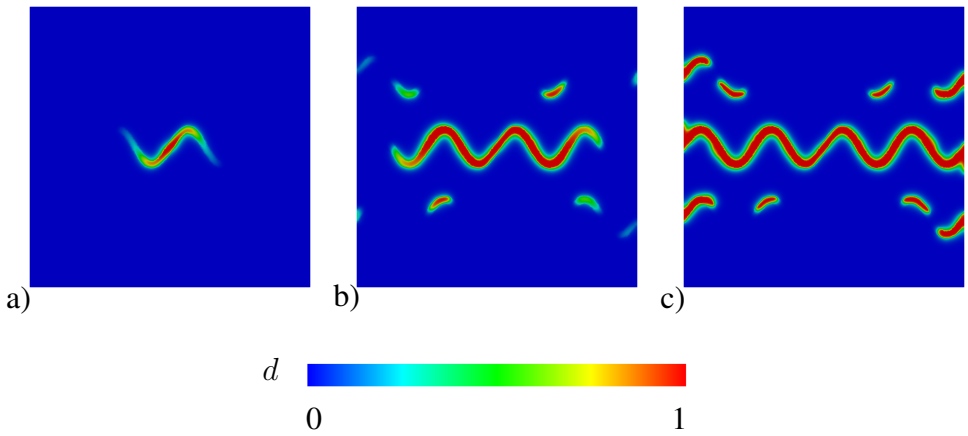

Figure 4.12: Tension test. Crack propogation for the sinusoidal interface at a load of (a) $F = 61.88$ N, (b) $F = 38.27$ N, (c) $F = 0$ N, see Figure 4.11.

4.2.2 Shear Test

This example involves a shear test performed on the same square plate as in the tension test. The geometry, dimensions, boundary conditions, and loading are shown in Figure 4.13. The plate is restrained horizontally and vertically at the bottom edge and vertically at the right and left edges. The domain is discretized with three-node triangular elements of effective element size $h = 0.1$ mm and length scale parameter $l = 0.2$ mm. The specimen is composed of 4 layers and we choose the interface thickness as 0.6 mm. The material parameters are given in Table 4.3.

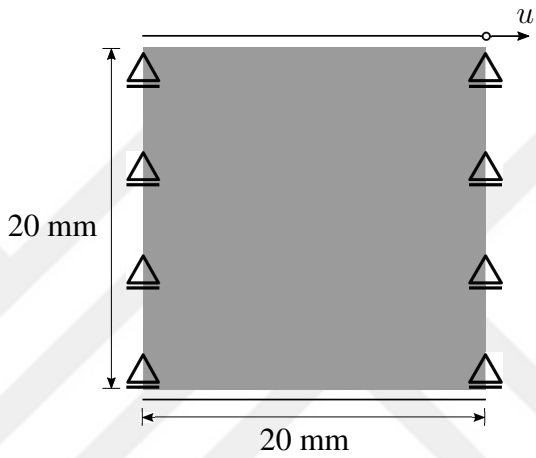

Figure 4.13: Geometry, dimensions, and boundary conditions for shear test.

Displacement-controlled loading is conducted by constantly increasing the displacement on the top surface with an increment of $\Delta u = 1 \times 10^{-5}$ mm. The phase-field profiles corresponding to the fully cracked state of the specimen with different interface patterns are given in Figure 4.14. In the specimen with the horizontal interface, cracks form at all the interfaces and the layers remain undamaged. In the specimens with the triangular and sinusoidal interface, the crack also propagates at all the interfaces; however, the cracks at the interfaces are linked through layers and some parts of the interfaces remain undamaged or partially damaged.

To evaluate the effect of the interface types on mechanical performance for the shear test, load-displacement curves for the different types of interface are plotted in Figure 4.15. It is observed that the ultimate load values do not depend on the interface type. However, the toughness of the specimens presented in Table 4.4 depends on the

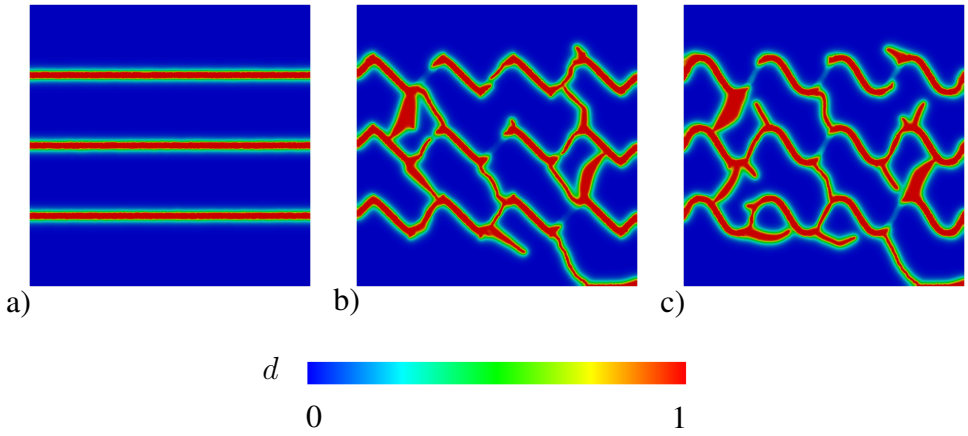

Figure 4.14: Shear test. Crack pattern for (a) horizontal, (b) triangular, and (c) sinusoidal interface types.

interface type. There is a 6.9% increase in toughness for the specimen possessing the sinusoidal interface and an 11.1% increase in toughness for the specimen possessing the triangular interface compared to the specimen possessing the horizontal interface.

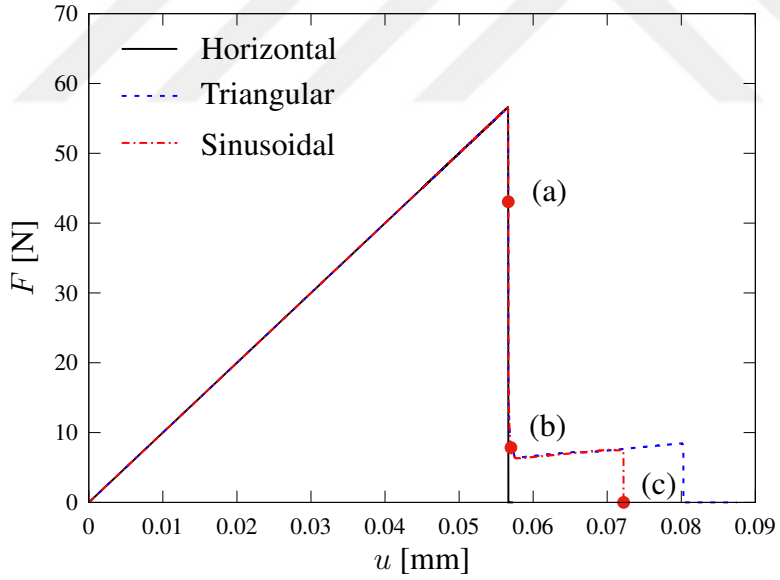

Figure 4.15: Shear test. Load-displacement curves for horizontal, triangular, and sinusoidal interface types.

For the specimen with the sinusoidal interface, the crack propagation patterns at different stages of loading are given in Figure 4.16 where the labels follow the marking

Table 4.4: Toughness values for the shear test

Interface type	Toughness [N-mm]
Horizontal	1.603
Triangular	1.781
Sinusoidal	1.714

in Figure 4.15. The crack begins to localize at the interfaces where the sinusoidal curve is decreasing and propagates through the layers linking the cracks at each interface.

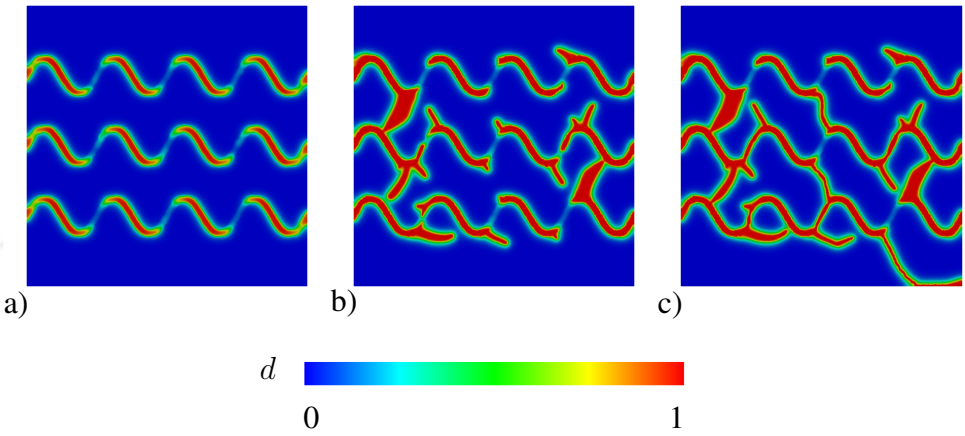

Figure 4.16: Shear test. Crack propogation for the sinusoidal interface at the load level of (a) $F = 43.06$ N, (b) $F = 7.86$ N, and (c) $F = 0$ N, see Figure 4.15.

4.2.2.1 Parameter Study

The cold joints (interfaces) between the layers can have various strength values due to diversity in size and distribution of voids in interfaces affected by the parameters such as the printing interval of the layers and the binder composition of the material. To address this issue, we perform a parameters study for the critical fracture energy

Ψ_c^i and the thickness of the interfaces in shear test.

For this purpose, displacement-driven loading is carried out by monotonically increasing the displacement on the top surface with a displacement increment of $\Delta u = 1 \times 10^{-5}$ mm. For the different values of the critical fracture energy Ψ_c^i of each interface type, the phase-field profiles, depicted in Figure 4.17, and the load-displacement curves, given in Figure 4.19, are obtained. For the different values of the thickness of each interface type, the phase-field profiles are given in Figure 4.18 and the corresponding load-displacement curves are shown in Figure 4.20.

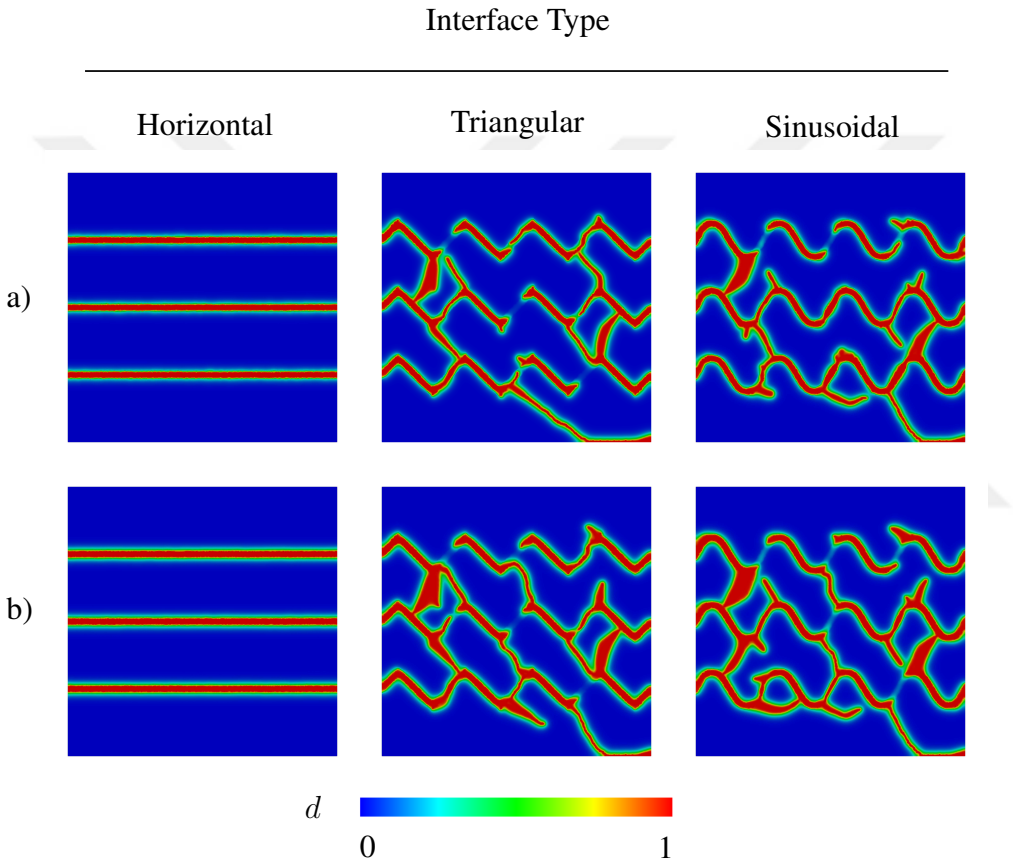

Figure 4.17: Shear test. Crack pattern for (a) $\Psi_c^i = 1.5$ kJ/m^3 , (b) $\Psi_c^i = 2.5$ kJ/m^3.

For all the interface types, the thickness of the cracks at the interfaces is increasing when the thickness of the interfaces is increasing and does not change by critical fracture energy of the interfaces Ψ_c^i. In the specimen with the horizontal interface, cracks occur at all the interfaces and the layers are undamaged regardless of the interface thickness and Ψ_c^i. In the specimens with the triangular and sinusoidal interface, the

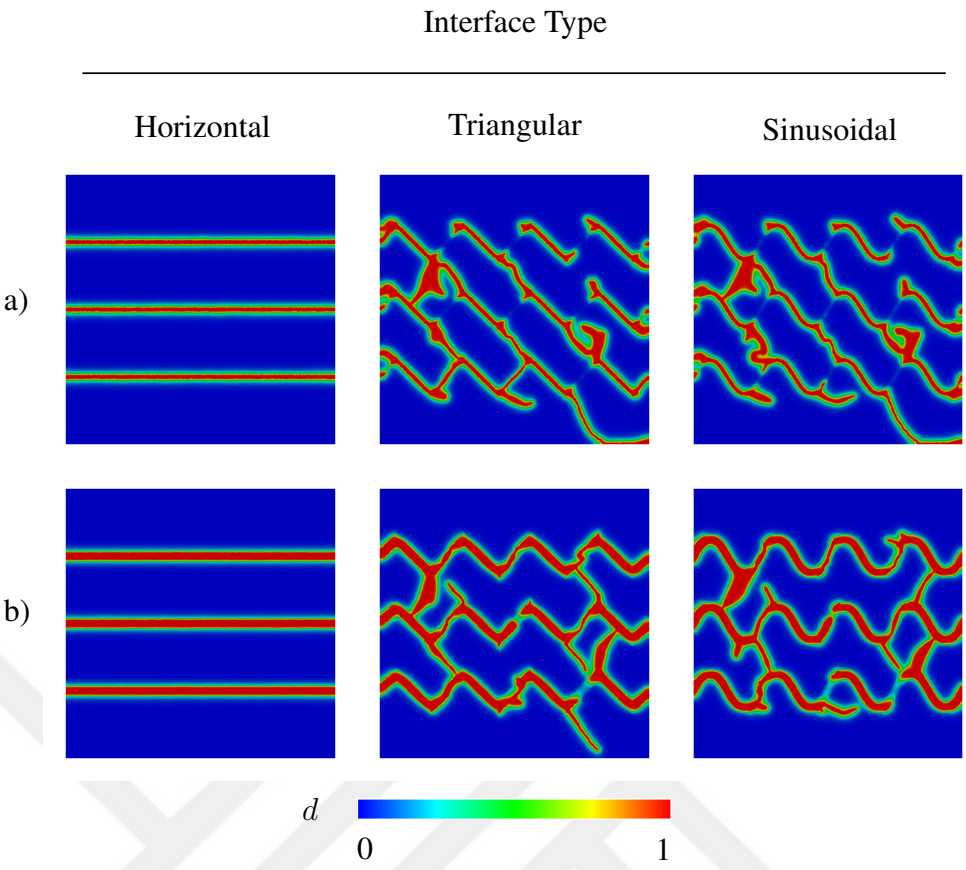

Figure 4.18: Shear test. Crack pattern for (a) 0.4 mm of interface thickness, (b) 0.8 mm of interface thickness.

crack propagates at interfaces and also in the layers regardless of the interface thickness and Ψ_c^i. However, when the interface thickness of the specimens is increasing, the crack tends to propagate more in the layers and less at the interfaces as shown in Figure 4.18.

Moreover, it is observed that for each interface type, the ultimate load of the specimens highly depends on the critical fracture energy of the interfaces Ψ_c^i but does not depend on the interface thickness as shown in Figures 4.19 and 4.20. The toughness values calculated from these curves are presented in Table 4.5 for the parameter study of critical fracture energy of interfaces Ψ_c^i and in Table 4.6 for the parameter study of interface thickness, and visualized in Figure 4.21 and Figure 4.22, respectively. For each interface type, the toughness of the specimens highly depends on the critical fracture energy of the interfaces Ψ_c^i.

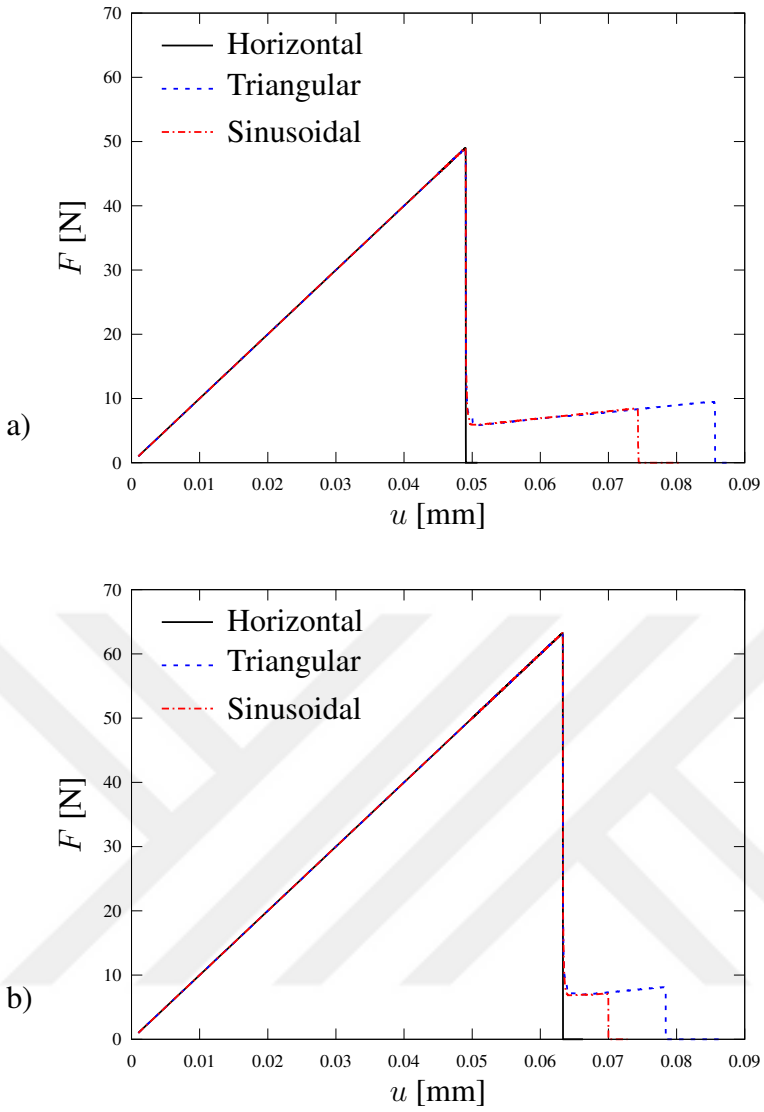

Figure 4.19: Shear test. Load-displacement curves for (a) $\Psi_c^i = 1.5$ kJ/m^3 , (b) $\Psi_c^i = 2.5$ kJ/m^3.

As the critical energy of the interfaces Ψ_c^i decreases, the effect of the interfaces on toughness becomes much more evident. In the specimens with $\Psi_c^i = 1.5$ kJ/m^3, there is a 15.1% increase in toughness for the specimens possessing sinusoidal interface and a 23.4% increase in toughness for the specimens possessing triangular interface compared to the specimens with the horizontal interface. In the specimens with $\Psi_c^i = 2.5$ kJ/m^3, there is a 2.4% increase in toughness for the specimens having sinusoidal interface and a 5.7% increase in toughness for the specimens possessing triangular interface compared to the specimens with the horizontal interface. The ef-

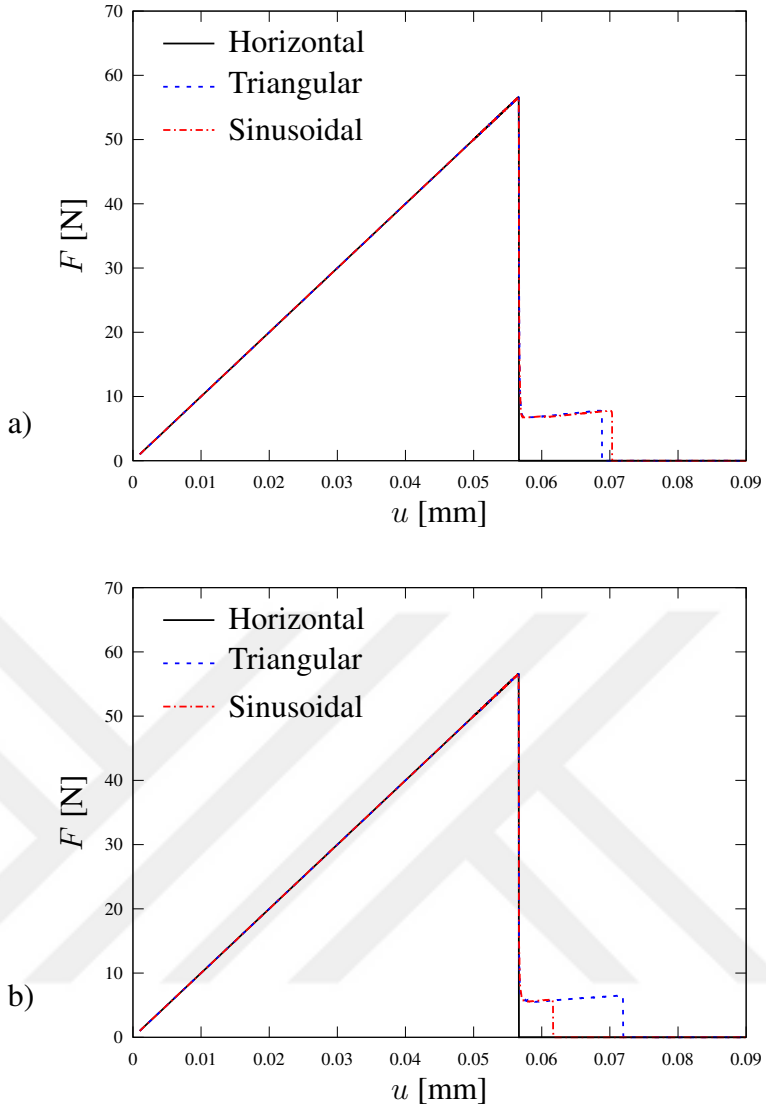

Figure 4.20: Shear test. Load-displacement curves for (a) 0.4 mm of interface thickness, (b) 0.8 mm of interface thickness.

fect of the interface thickness on the toughness of the specimens is less significant and non-proportional. In the specimens with horizontal interface, the interface thickness does not influence the toughness of the specimens. However, in the specimens with triangular interface and sinusoidal interface, the toughness of the specimens fluctuates with respect to interface thickness. This may indicate the existence of an optimum ratio of the interface thickness to the layer thickness.

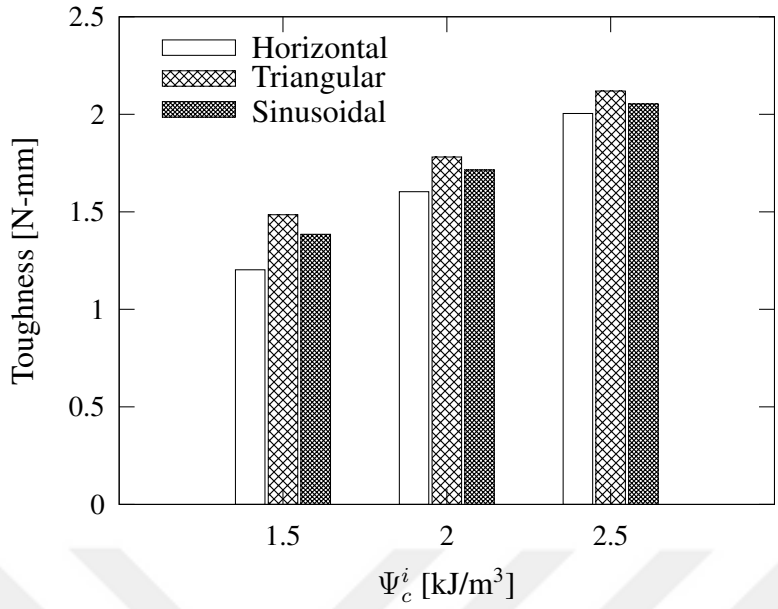

Figure 4.21: Parameter study for 0.6 mm interface thickness. Toughness values for the shear test.

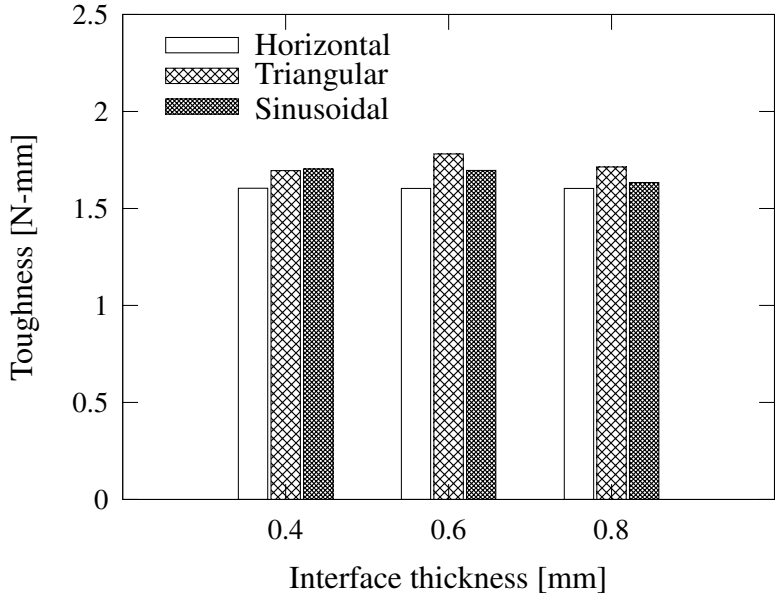

Figure 4.22: Parameter study for 2 kJ/m^3 Ψ_c^i. Toughness values for the shear test.

Table 4.5: Parameter study for 0.6 mm interface thickness. Toughness values for the shear test.

Specified parameter	Interface type	Toughness [N-mm]
$\Psi_c^i = 1.5$ kJ/m^3	Horizontal	1.203
	Triangular	1.485
	Sinusoidal	1.385
$\Psi_c^i = 2.0$ kJ/m^3	Horizontal	1.603
	Triangular	1.781
	Sinusoidal	1.714
$\Psi_c^i = 2.5$ kJ/m^3	Horizontal	2.004
	Triangular	2.119
	Sinusoidal	2.053

Table 4.6: Parameter study for 2 kJ/m^3 critical fracture energy Ψ_c^i. Toughness values for the shear test.

Specified parameter	Interface type	Toughness [N-mm]
Thickness $= 0.4$ mm	Horizontal	1.604
	Triangular	1.695
	Sinusoidal	1.704
Thickness $= 0.6$ mm	Horizontal	1.603
	Triangular	1.781
	Sinusoidal	1.714
Thickness $= 0.8$ mm	Horizontal	1.603
	Triangular	1.696
	Sinusoidal	1.634

4.2.3 Bending Test

This example involves three-point and four-point bending tests of a notched beam with various layer configurations presented in Figure 4.9. The beam is composed of 5 layers and we choose the interface thickness as 0.6 mm. The values of the material parameters are given in Table 4.3.

4.2.3.1 Three-Point Bending Test

The geometry, dimensions, boundary conditions, and loading used in the three-point bending test are shown in Figure 4.23. The domain is discretized using three-node triangular elements of effective element size $h = 0.15$ mm and the length-scale parameter $l = 0.3$ mm.

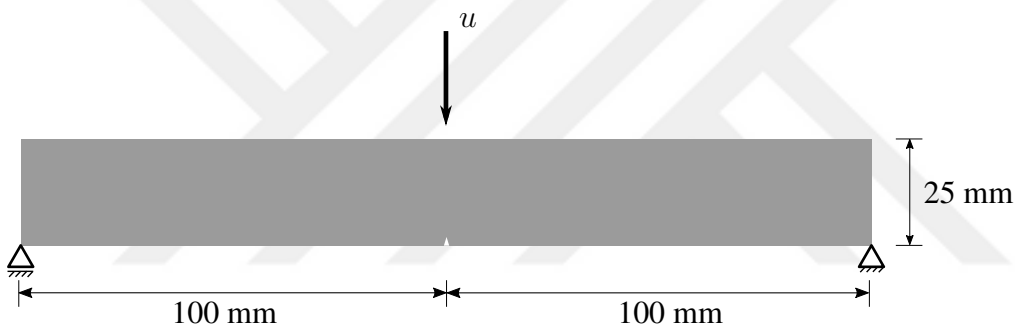

Figure 4.23: Geometry, dimensions, and boundary conditions for three-point bending test.

Displacement-controlled loading is performed by constantly increasing the displacement at the center of the top surface of the beam with an increment of $\Delta u = 5 \times 10^{-5}$ mm. The crack patterns at the ultimate failure are given in Figure 4.24. The crack tends to expand to the sides of the specimen through the interfaces much more in the specimen with horizontal interface than the specimens with triangular and sinusoidal interfaces.

To evaluate the effect of the interface types on mechanical performance for the bending test, load-displacement curves for each interface type are plotted in Figure 4.25. It is observed that the interface types have no effect on mechanical performance in

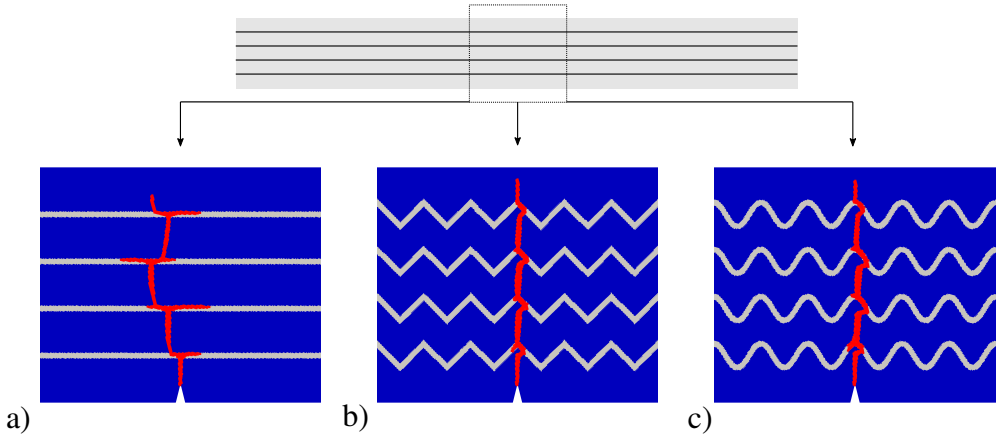

Figure 4.24: Three-point bending test. Crack pattern for (a) horizontal, (b) triangular, and (c) sinusoidal interface. Blue represents layers, white shows interfaces, and red depicts the crack.

the three-point bending test as the curves for each interface type almost coincide.

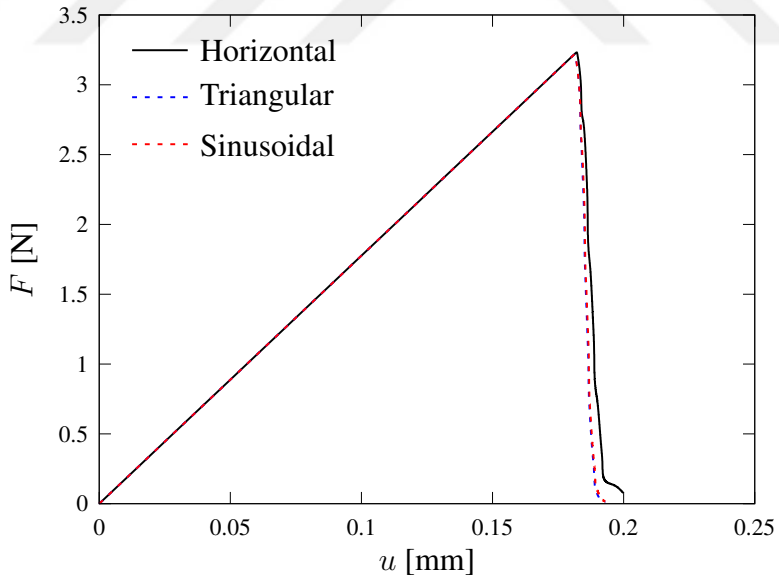

Figure 4.25: Three-point bending test. Load-displacement curves for horizontal, triangular, and sinusoidal interface types.

4.2.3.2 Four-Point Bending Test

The geometry, dimensions, boundary conditions, and loading used in the four-point bending test are shown in Figure 4.26. The domain is discretized using three-node triangular elements of effective element size $h = 0.15$ mm and length scale parameter $l = 0.3$ mm.

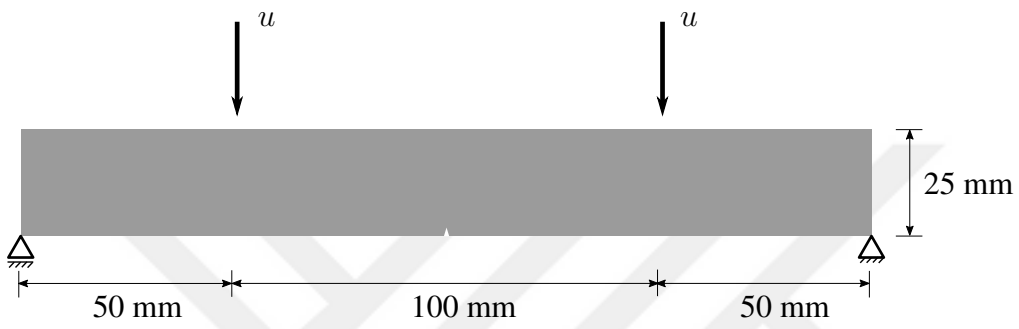

Figure 4.26: Geometry, dimensions, and boundary conditions for four-point bending test.

Displacement-controlled loading is performed by constantly increasing the displacement at two points located 25 mm apart from the side edges symmetrically positioned at the top surface of the beam with an increment of $\Delta u = 5 \times 10^{-5}$ mm. The crack patterns at the ultimate failure are given in Figure 4.27. The crack tends to expand to the sides of the specimen through the interfaces much more in the specimen with horizontal interface than the specimens with triangular and sinusoidal interfaces. The crack width is wider for all the interface types in the four-point bending test than that in the three-point bending test.

To evaluate the effect of the interface types on mechanical performance for the bending test, load-displacement curves for each interface type are plotted in Figure 4.28. It is observed that the interface types have no effect on mechanical performance in the four-point bending test as the curves for each interface type almost coincide.

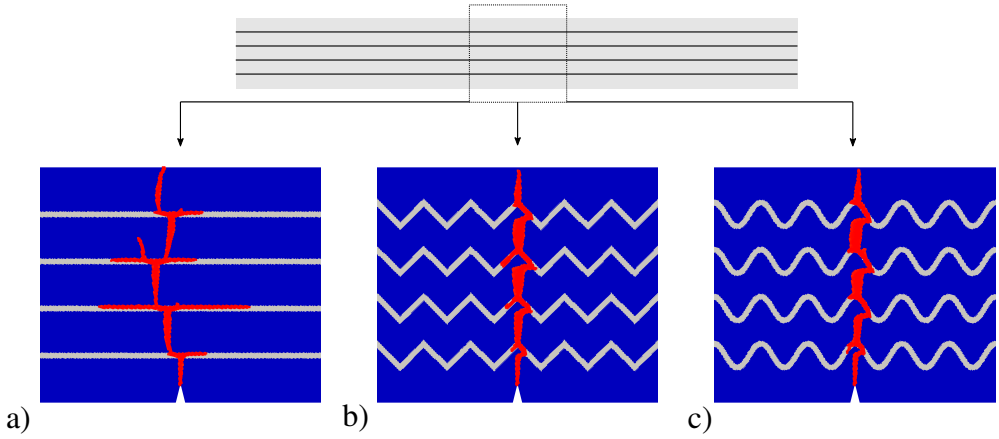

Figure 4.27: Four-point bending test. Crack pattern for (a) horizontal, (b) triangular, and (c) sinusoidal interface types.

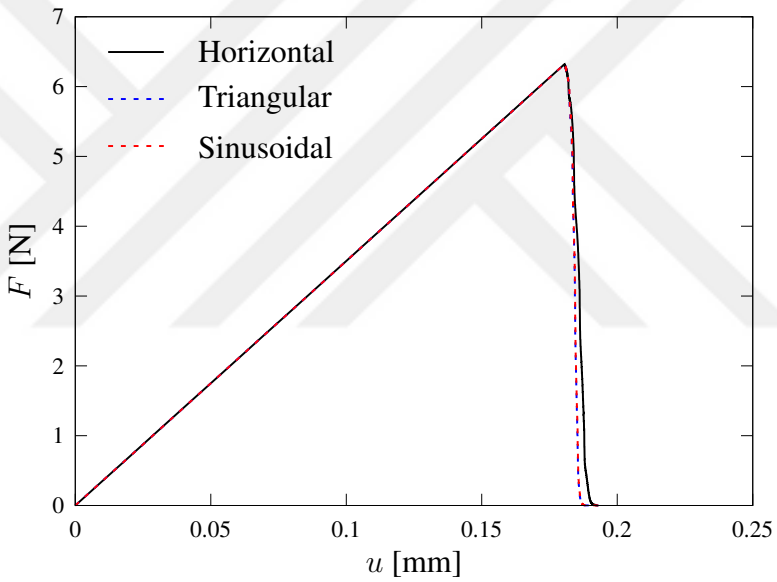

Figure 4.28: Four-point bending test. Load-displacement curves for horizontal, triangular, and sinusoidal interface types.

4.2.4 Lateral Loading

This example involves a lateral loading test performed on the same square plate as the one in the tension and shear test. The geometry, dimensions, boundary conditions, and loading are shown in Figure 4.29. The plate is restrained horizontally and vertically at the bottom edge and vertically at the top, right and left edges. The domain is

discretized using three-node triangular elements of effective element size $h = 0.1$ mm and length scale parameter $l = 0.2$ mm. The specimen is composed of 4 layers and we choose the interface thickness as 0.6 mm. The material parameters are given in Table 4.3.

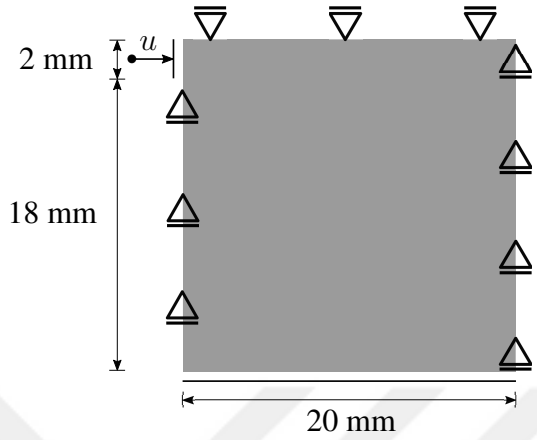

Figure 4.29: Geometry, dimensions and boundary conditions for lateral loading test.

Displacement-controlled loading is performed by constantly increasing the displacement on the top-left surface with an increment of $\Delta u = 1 \times 10^{-5}$ mm. The crack patterns at the ultimate failure are given in Figure 4.30. The left parts of the cracks are diagonal for all the interfaces to the point where the crack is at the bottom interface of the specimen; however, from that point on, the right side of the crack differs. For the specimen with the horizontal interface, the crack is at the bottom interface of the specimen while for the specimens with triangular and sinusoidal interfaces, only a little portion of the crack is at the bottom interface and the remaining portion is at the bottom layer of the specimen. The crack propagates diagonally for all the interface types; however in the specimen with the horizontal interface, it continues to propagate through the bottom interface while in the specimens with triangular and sinusoidal interfaces, the crack continues to propagate through the layer at the bottom.

To evaluate the effect of the interface types on mechanical performance for the lateral test, load-displacement curves for each interface type are plotted in Figure 4.31. It is observed that there is a slight increase in the ultimate load of the specimens having triangular and sinusoidal interfaces compared to the specimen having the horizontal interface in the lateral loading test.

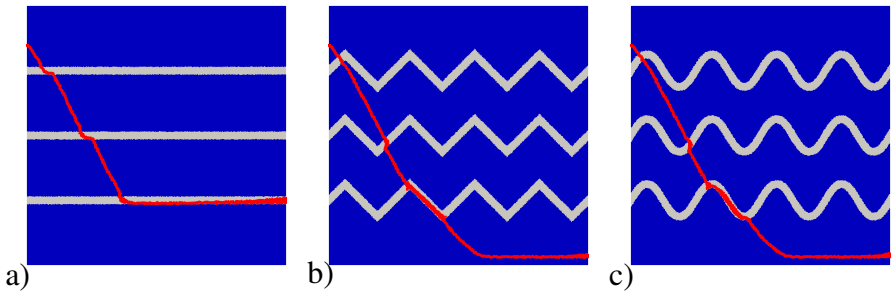

Figure 4.30: Lateral loading test. Crack pattern for (a) horizontal, (b) triangular, and (c) sinusoidal interface types.

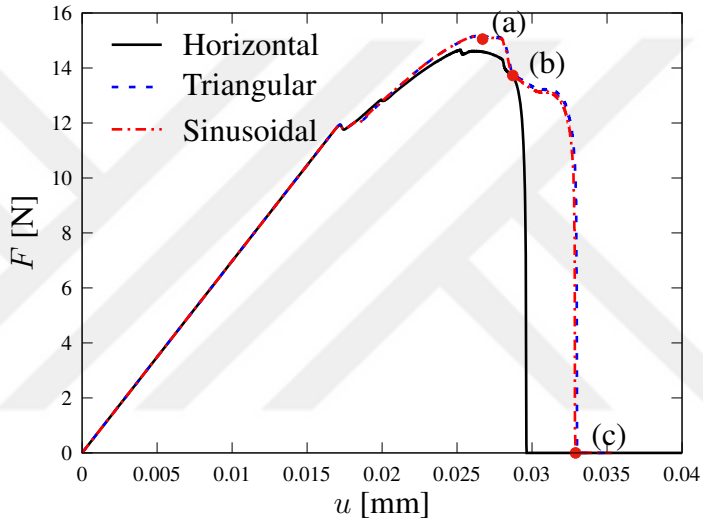

Figure 4.31: Lateral loading test. Load-displacement curves for horizontal, triangular, and sinusoidal interface types.

The toughness values calculated from these curves are presented in Table 4.7. There is a 16.7% increase in toughness for the specimen possessing the sinusoidal interface and a 17.4% increase in toughness for the specimen possessing the triangular interface compared to the specimen having the horizontal interface. For the specimen with the sinusoidal interface, the crack propagation patterns at different stages of the loading are given in Figure 4.32 where the labels refer to that in Figure 4.31. The crack begins to propagate diagonally at the upper left part of the specimen and continues to propagate through the bottom layer of the specimen.

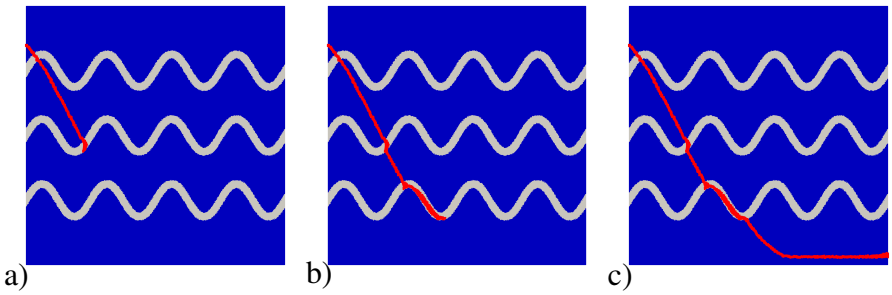

Figure 4.32: Lateral loading test. Crack propogation for the sinusoidal interface at a load of (a) $F = 15.05$ N, (b) $F = 13.73$ N, and (c) $F = 0$ N, see Figure 4.31.

Table 4.7: Toughness values for the lateral loading test

Interface type	Toughness [N-mm]
Horizontal	0.270
Triangular	0.317
Sinusoidal	0.315

4.2.5 Masonry Wall

In this section, the proposed modeling approach is applied to masonry wall structures. Masonry structures are composed of bricks and these bricks are bound together by mortar resulting in interfaces between the bricks. As in additively manufactured concrete, the interfaces have lower strength than their surrounding parts. Thus, we will analyze the masonry shear wall in [74] to test the capacity of the model. The bond type between the bricks used in the wall is a running bond where the bricks of the corresponding layers are staggered by half-size of a brick compared to the layers above and below it as depicted in Figure 4.34. The bricks used in the experiment were Joosten solid clay bricks that are 210 mm in length, 50 mm in height, and 98 mm in width. The bricks are bonded with a mortar of 10 mm thickness. The 70-millimeter top and bottom of the wall are clamped with steel beams. The geometry, dimensions,

boundary conditions, and loading are shown in Figure 4.33. Also, the side edges of the wall are restrained in vertical direction by roller supports as depicted in Figure 4.33. The domain is discretized with three-node triangular elements of effective element size $h = 2.5$ mm and the length scale parameter is taken as $l = 5$ mm. The values of the material parameters are given in Table 4.8. The interface thickness and the material parameters are adapted from the studies [75–77].

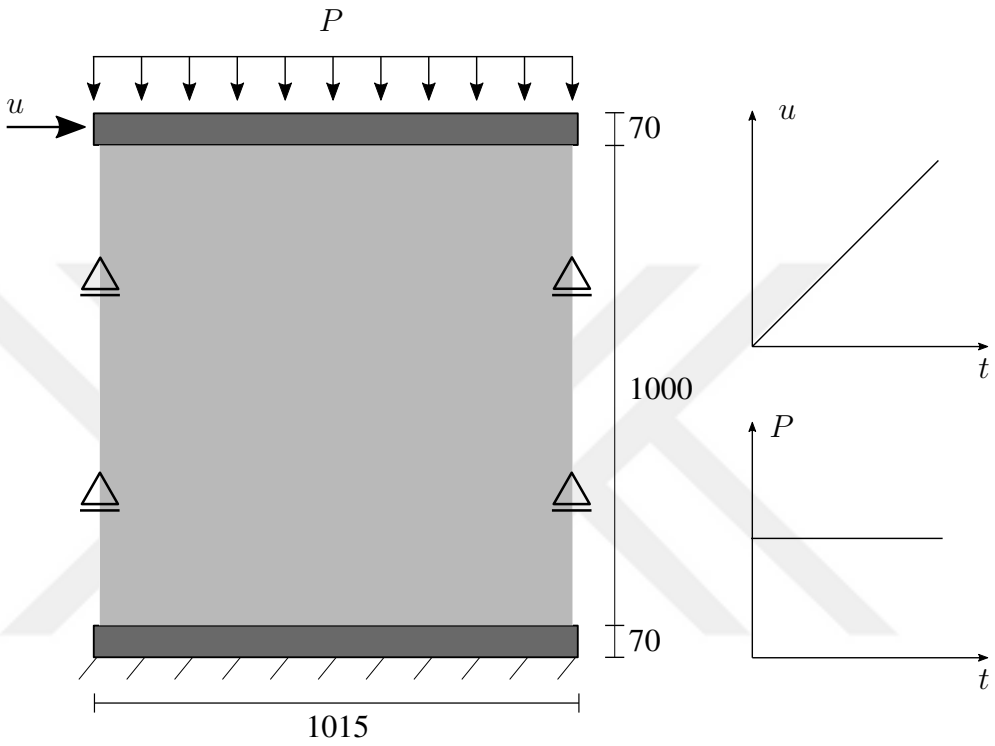

Figure 4.33: Geometry, dimensions, and boundary conditions for masonry shear wall test. Units are in mm.

30 kN pre-compression load equivalent to the distributed load of 0.30 MPa is applied to the top surface of the upper steel beam. Displacement-driven loading is achieved by monotonically increasing the displacement on the left surface of the upper steel beam with a displacement increment of $\Delta u = 1 \times 10^{-3}$ mm. The crack pattern obtained by the model along with the experimental crack pattern is given in Figure 4.34. The numerical model predicts diagonal and "step-like" crack pattern obtained by the experiment.

The crack pattern for the same analysis of the masonry wall when the roller supports

Table 4.8: Material parameters for the masonry wall

Parameter	Description	Unit	Value
Ψ_c^l	Critical fracture energy for bricks	kJ/m^3	8
Ψ_c^i	Critical fracture energy for mortar	kJ/m^3	1.6
E	Elastic modulus	GPa	3.15
ν	Poisson's ratio	-	0.14
ζ	Driving force slope	-	15

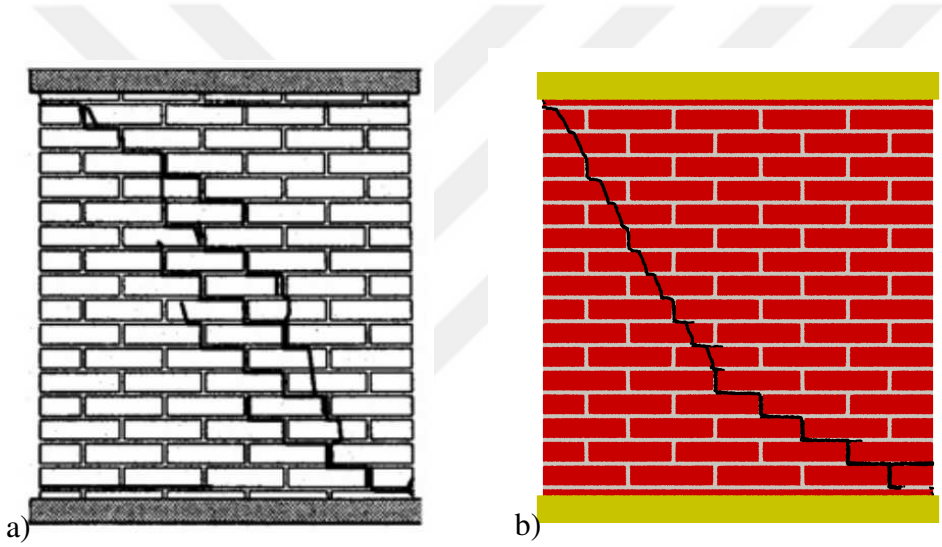

Figure 4.34: Masonry shear wall test. Crack pattern for masonry wall obtained (a) experimentally, and (b) numerically.

at the side edges of the wall are not present is given in Figure 4.35. In that case, the crack pattern is not realistic as only the mortar at the top interface cracks. Therefore, we continue with the case where the side edges of the wall are restrained vertically.

The load-displacement curves from the numerical model along with the experimental test are given in Figure 4.36. It is observed that the numerical model captures the initial stiffness and nonlinearity of the load-displacement curve from the experiment. However, it produces more brittle behavior than the experiment, may be caused by

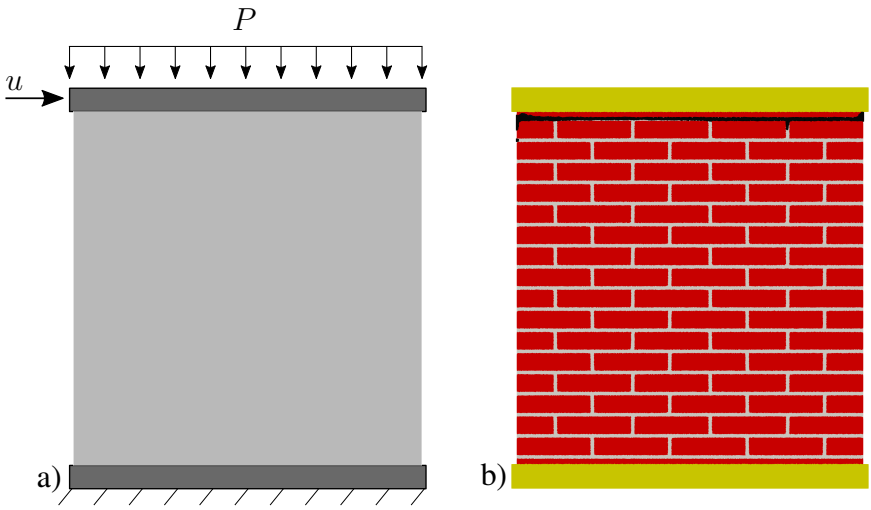

Figure 4.35: Masonry shear wall test without roller supports at the side edges. (a) Geometry, dimensions, and boundary conditions. (b) Crack pattern.

the isotropic degradation of the stress tensor and overshoots the ultimate load, may be caused by the plain strain assumption of the model.

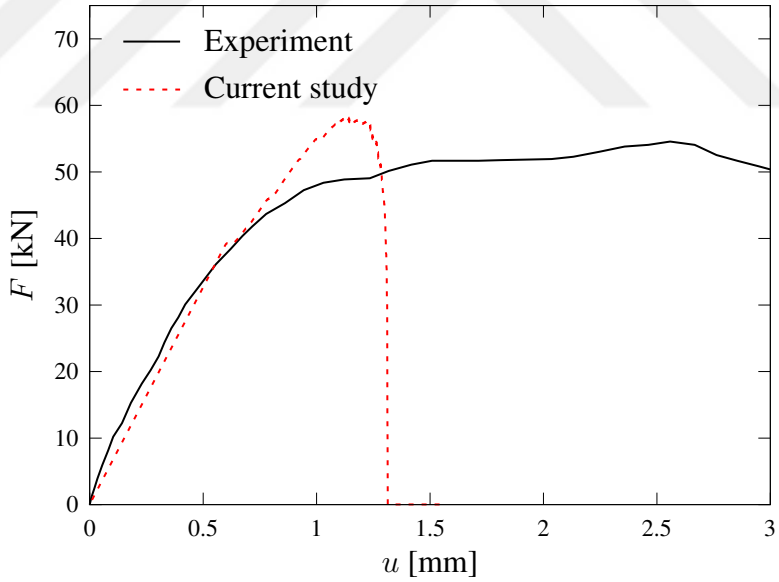

Figure 4.36: Masonry shear wall test. Comparison of experimental and numerical load-displacement curves.

In the tests on additively manufactured concrete, we analyzed different types of interfaces and concluded that the interface type has a significant effect on the mechanical

performance and toughness of the specimen under certain loading conditions. To further validate this effect, we investigate the effect of the bond type between the bricks on the mechanical performance of the masonry walls. We use a masonry wall with stack bond where the bricks are stacked on top of each other without staggering in addition to the masonry wall with running bond as in the previous example as shown in Figure 4.37. The geometry, dimensions, boundary conditions, and loading are shown in Figure 4.33. The domain is discretized with three-node triangular elements of effective element size $h = 2.5$ mm and the length scale parameter is taken as $l = 5$ mm. The values of the material parameters are given in Table 4.8.

Displacement-driven loading is conducted by monotonically increasing the displacement on the left surface of the upper steel beam with a displacement increment of $\Delta u = 1 \times 10^{-3}$ mm. The crack pattern for each masonry wall is given in Figure 4.37. The crack tends to propagate in mortar more in the masonry wall with stack bond than running bond.

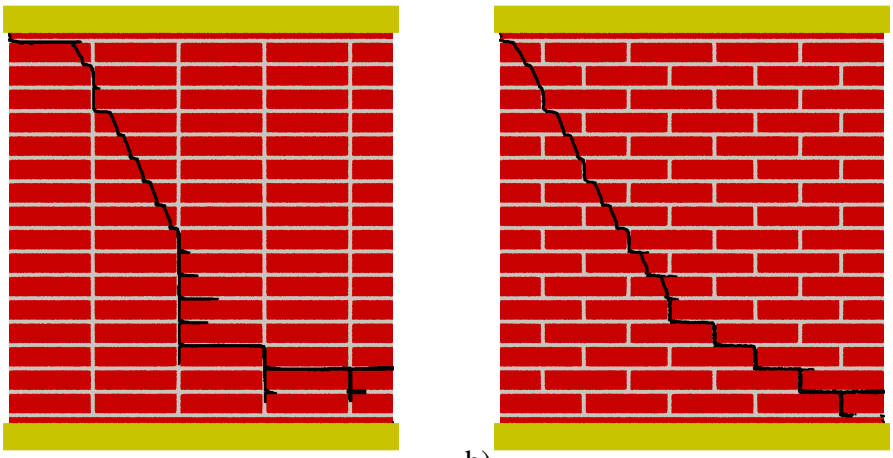

Figure 4.37: Masonry shear wall test. Crack pattern for masonry wall with (a) stack bond, and (b) running bond.

To evaluate the effect of the bond types on the mechanical performance of the masonry wall, load-displacement curves for each bond type are plotted in Figure 4.38. It is observed that there is a considerable decrease in the ultimate load of the masonry wall with stack bond compared to the masonry wall with running bond as shown in Figure 4.38.

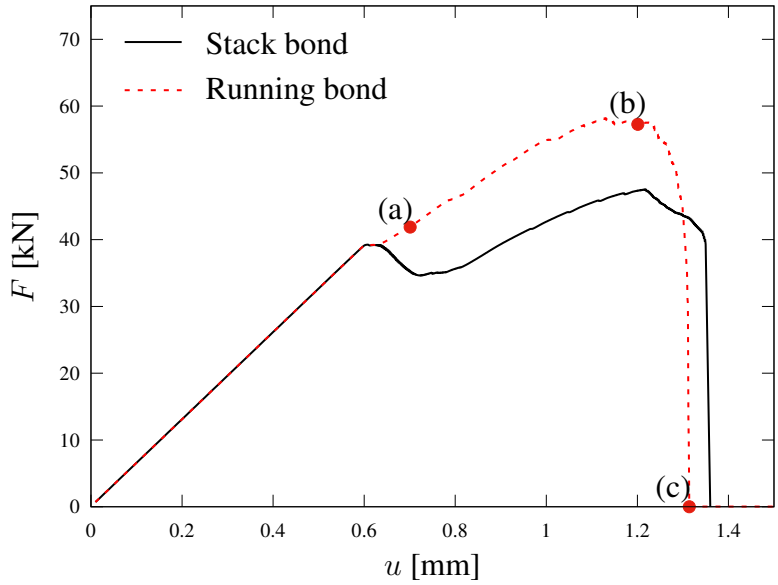

Figure 4.38: Masonry shear wall test. Load-displacement curves for masonry walls with stack bond and running bond.

Table 4.9: Toughness values for the masonry shear wall test

Interface type	Toughness [N-m]
Stack bond	42.84
Running bond	47.60

The toughness values calculated from these curves are presented in Table 4.9. There is a 10% decrease in toughness for the masonry wall with stack bond compared to that with running bond.

For the masonry wall with running bond, the crack propagation patterns at different stages of loadings are given in Figure 4.39 where the labeling follows from the one used in Figure 4.38. The crack begins to localize at the top-left corner of the wall and propagates diagonally with a "step-like" pattern. In the beginning, the crack propagates more on the bricks while later, it propagates more on the mortar.

Also, the masonry wall with running bond is analyzed with a 610 mm square opening

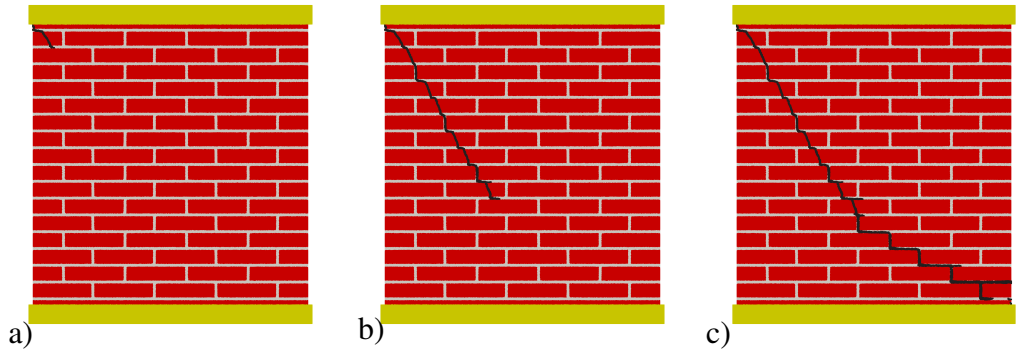

Figure 4.39: Masonry shear wall test. Crack propogation for the masonry wall with running bond at the load level of (a) $F = 41.88$ kN, (b) $F = 57.27$ kN, and (c) $F = 0$ kN, see Figure 4.38.

in its center. The crack pattern for masonry walls with and without opening is given in Figure 4.40. Unlike the masonry wall without an opening, only the mortars at the top-left and bottom-right of the opening crack horizontally in the masonry wall with an opening. This is in accord with the observations in real-life conditions as illustrated in Figure 4.41.

The same masonry wall with running bond is further analyzed with ground settlement and heave conditions as shown in Figure 4.42. Displacement-driven loading is conducted by monotonically increasing the displacement on the left part of the bottom surface of the wall with a displacement increment of $\Delta u = 1 \times 10^{-3}$ mm.

The crack pattern for each condition is given in Figure 4.43. In the condition with ground settlement, a crack occurs from the middle part of the bottom surface of the wall to the left surface of the wall through the bottom mortar. On the other hand, in the condition with ground heave, a crack occurs from the middle part of the bottom surface of the wall to the right surface of the wall through the bottom mortar.

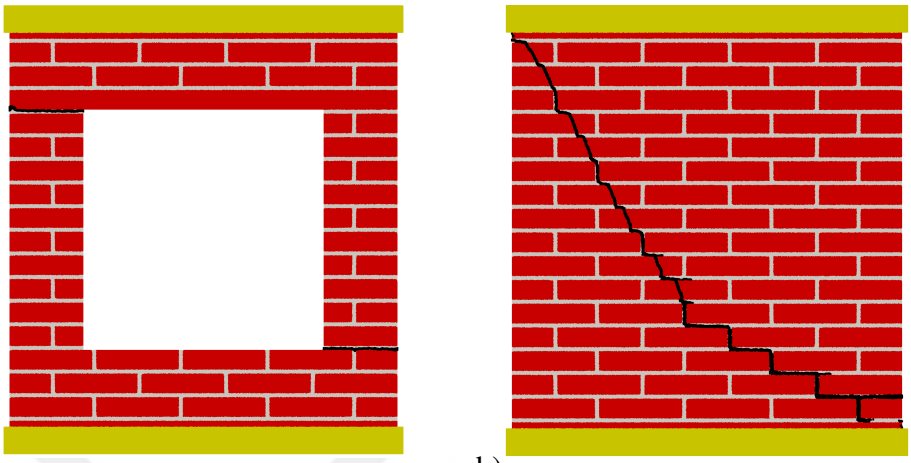

a) b)

Figure 4.40: Masonry shear wall test. Crack pattern for masonry wall (a) with and (b) without openings.

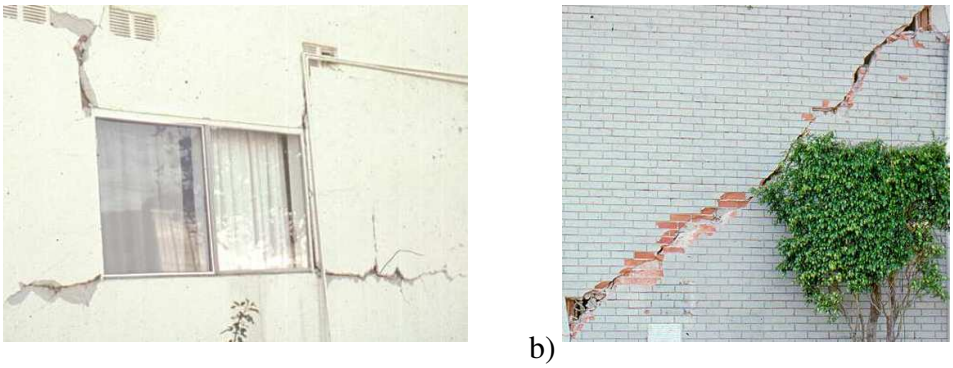

a) b)

Figure 4.41: Masonry structures (a) with and (b) without openings adopted from [78].

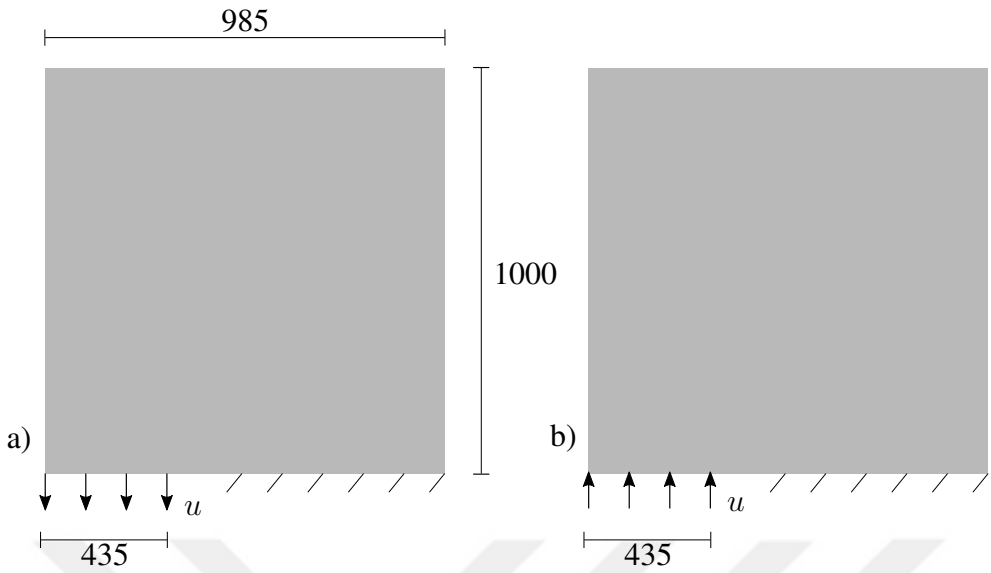

Figure 4.42: Geometry, dimensions, and boundary conditions for masonry wall with (a) ground settlement, and (b) ground heave conditions. Units are in mm.

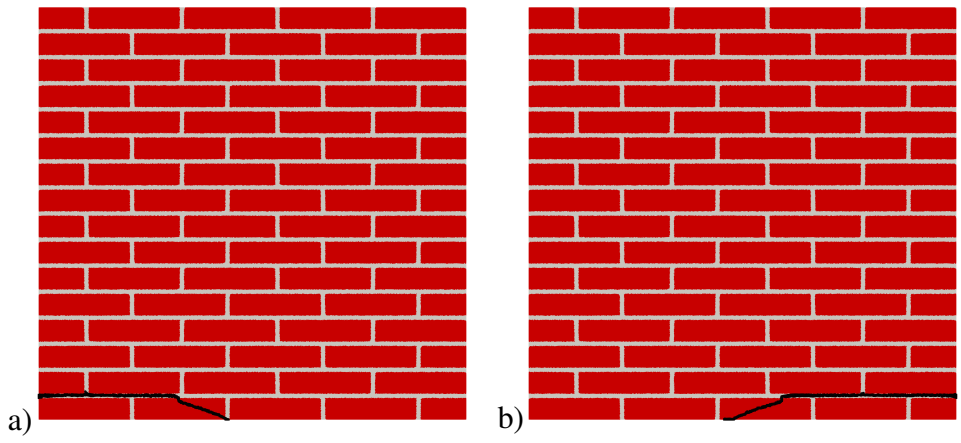

Figure 4.43: Masonry shear wall test. Crack pattern for masonry wall with boundary conditions (a) ground settlement, and (b) ground heave.

CHAPTER 5

CONCLUDING REMARKS

In this study, the phase-field modeling of cracking in additively manufactured concrete with a subsequent extension of the developed modeling approach to masonry wall structures has been investigated. For this purpose, a phase-field modeling framework based on the studies of Miehe et al. [26] and Ambati et al. [28] has been established. For the evolution of phase-field, a strain criterion with threshold from [26] has been adopted to generate length-scale independent results, and hybrid formulation from [28] has been incorporated to differentiate between tensile and compressive damaging modes without increasing the computational cost compared to the isotropic formulation.

The validation of the model is performed with several examples, including experimental validations. While it substantially captures the crack patterns and the mechanical behavior from experimental data, further considerations are necessary to improve its accuracy and capacity. In masonry wall structures, it generates much more brittle behavior than the experiments. Therefore, in future studies, the isotropic degradation of the stress tensor should be replaced with other techniques by agreeing to an increase in computational cost. Moreover, damaging modes other than tensile fracture (Mode I) should be considered to be able to generate more accurate crack patterns and increase the predictive capacity of the model.

The model is applied to numerical examples using several specimens and boundary conditions to investigate the mechanical behavior of additively manufactured concrete and masonry walls undergoing cracking. For the additively manufactured concrete specimens, different types of interfaces, namely horizontal, triangular, and sinusoidal, have been considered to examine the effect of the interface types on the mechanical

performance and toughness of the specimens. In tension and bending tests, no significant effect on the toughness of the specimens by the interface type has been observed other than the expansion of the cracks to the sides of the specimen with horizontal interface in bending tests. However, in shear and lateral loading tests, the toughness of specimens with triangular and sinusoidal interface have been higher compared to that with horizontal interface. Also, a parameters study is conducted to examine the effect of the parameters critical fracture energy of interfaces Ψ_c^i and the thickness of the interfaces. It is observed that the effect of Ψ_c^i on mechanical performance and toughness of the specimens is much higher than the effect of interface thickness. In future studies, it should be considered to extend these 2D applications to 3D to be able to model structures with geometries depending upon three dimensions more accurately. Also, different geometrical configurations in 3D should be considered for the interfaces to create structures with higher strength and toughness. For masonry wall structures, the effect of different bond types and different loading and boundary conditions on mechanical behavior and crack patterns are investigated to further validate the capacity of the model.

To conclude, a robust computational model is developed by addressing the lack of studies existing in the literature computationally modeling the mechanical behavior of additively manufactured concrete undergoing cracking. Moreover, the modeling performance of the proposed approach in modeling masonry wall structures can also be applied to the analysis of historic masonry structures. This study contributes to research advances in additive manufacturing, particularly in the field of fracture mechanics and the construction industry by extending the existing literature.

REFERENCES

[1] I. Gibson, D. Rosen, and B. Stucker, *Additive Manufacturing Technologies: 3D Printing, Rapid Prototyping, and Direct Digital Manufacturing*. Springer New York, 2014.

[2] R. Wolfs, F. Bos, and T. Salet, "Hardened properties of 3D printed concrete: The influence of process parameters on interlayer adhesion," *Cement and Concrete Research*, vol. 119, pp. 132–140, 2019.

[3] G. A. Francfort and J.-J. Marigo, "Revisiting brittle fracture as an energy minimization problem," *Journal of the Mechanics and Physics of Solids*, vol. 46, no. 8, pp. 1319–1342, 1998.

[4] B. Bourdin, G. A. Francfort, and J.-J. Marigo, "The variational approach to fracture," *Journal of elasticity*, vol. 91, pp. 5–148, 2008.

[5] C. Miehe, F. Welschinger, and M. Hofacker, "Thermodynamically consistent phase-field models of fracture: Variational principles and multi-field FE implementations," *International journal for numerical methods in engineering*, vol. 83, no. 10, pp. 1273–1311, 2010.

[6] C. Miehe, M. Hofacker, and F. Welschinger, "A phase field model for rate-independent crack propagation: Robust algorithmic implementation based on operator splits," *Computer Methods in Applied Mechanics and Engineering*, vol. 199, no. 45-48, pp. 2765–2778, 2010.

[7] H. Amor, J.-J. Marigo, and C. Maurini, "Regularized formulation of the variational brittle fracture with unilateral contact: Numerical experiments," *Journal of the Mechanics and Physics of Solids*, vol. 57, no. 8, pp. 1209–1229, 2009.

[8] G. Lancioni and G. Royer-Carfagni, "The variational approach to fracture mechanics. A practical application to the French Panthéon in Paris," *Journal of elasticity*, vol. 95, pp. 1–30, 2009.

[9] M. J. Borden, T. J. Hughes, C. M. Landis, and C. V. Verhoosel, "A higher-order phase-field model for brittle fracture: Formulation and analysis within the isogeometric analysis framework," *Computer Methods in Applied Mechanics and Engineering*, vol. 273, pp. 100–118, 2014.

[10] S. Natarajan, R. K. Annabattula, E. Martínez-Pañeda, *et al.*, "Phase field modelling of crack propagation in functionally graded materials," *Composites Part B: Engineering*, vol. 169, pp. 239–248, 2019.

[11] F. P. Duda, A. Ciarbonetti, P. J. Sánchez, and A. E. Huespe, "A phase-field/gradient damage model for brittle fracture in elastic–plastic solids," *International Journal of Plasticity*, vol. 65, pp. 269–296, 2015.

[12] R. Alessi, J.-J. Marigo, and S. Vidoli, "Gradient damage models coupled with plasticity: variational formulation and main properties," *Mechanics of Materials*, vol. 80, pp. 351–367, 2015.

[13] M. J. Borden, T. J. Hughes, C. M. Landis, A. Anvari, and I. J. Lee, "A phase-field formulation for fracture in ductile materials: Finite deformation balance law derivation, plastic degradation, and stress triaxiality effects," *Computer Methods in Applied Mechanics and Engineering*, vol. 312, pp. 130–166, 2016.

[14] C. V. Verhoosel and R. De Borst, "A phase-field model for cohesive fracture," *International Journal for numerical methods in Engineering*, vol. 96, no. 1, pp. 43–62, 2013.

[15] S. May, J. Vignollet, and R. De Borst, "A numerical assessment of phase-field models for brittle and cohesive fracture: γ-convergence and stress oscillations," *European Journal of Mechanics-A/Solids*, vol. 52, pp. 72–84, 2015.

[16] T.-T. Nguyen, J. Yvonnet, Q.-Z. Zhu, M. Bornert, and C. Chateau, "A phase-field method for computational modeling of interfacial damage interacting with crack propagation in realistic microstructures obtained by microtomography," *Computer Methods in Applied Mechanics and Engineering*, vol. 312, pp. 567–595, 2016.

[17] J. Vignollet, S. May, R. De Borst, and C. V. Verhoosel, "Phase-field models for brittle and cohesive fracture," *Meccanica*, vol. 49, pp. 2587–2601, 2014.

[18] C. J. Larsen, C. Ortner, and E. Süli, "Existence of solutions to a regularized model of dynamic fracture," *Mathematical Models and Methods in Applied Sciences*, vol. 20, no. 07, pp. 1021–1048, 2010.

[19] B. Bourdin, C. J. Larsen, and C. L. Richardson, "A time-discrete model for dynamic fracture based on crack regularization," *International journal of fracture*, vol. 168, pp. 133–143, 2011.

[20] M. Hofacker and C. Miehe, "Continuum phase field modeling of dynamic fracture: variational principles and staggered FE implementation," *International journal of fracture*, vol. 178, pp. 113–129, 2012.

[21] M. Hofacker and C. Miehe, "A phase field model of dynamic fracture: Robust field updates for the analysis of complex crack patterns," *International Journal for Numerical Methods in Engineering*, vol. 93, no. 3, pp. 276–301, 2013.

[22] A. Schlüter, A. Willenbücher, C. Kuhn, and R. Müller, "Phase field approximation of dynamic brittle fracture," *Computational Mechanics*, vol. 54, pp. 1141–1161, 2014.

[23] J. Bleyer, C. Roux-Langlois, and J.-F. Molinari, "Dynamic crack propagation with a variational phase-field model: limiting speed, crack branching and velocity-toughening mechanisms," *International Journal of Fracture*, vol. 204, no. 1, pp. 79–100, 2017.

[24] C. Miehe and L.-M. Schänzel, "Phase field modeling of fracture in rubbery polymers. Part I: Finite elasticity coupled with brittle failure," *Journal of the Mechanics and Physics of Solids*, vol. 65, pp. 93–113, 2014.

[25] C. Hesch and K. Weinberg, "Thermodynamically consistent algorithms for a finite-deformation phase-field approach to fracture," *International Journal for Numerical Methods in Engineering*, vol. 99, no. 12, pp. 906–924, 2014.

[26] C. Miehe, L.-M. Schänzel, and H. Ulmer, "Phase field modeling of fracture in multi-physics problems. Part I. Balance of crack surface and failure criteria for brittle crack propagation in thermo-elastic solids," *Computer Methods in Applied Mechanics and Engineering*, vol. 294, pp. 449–485, 2015.

[27] A. Raina and C. Miehe, "A phase-field model for fracture in biological tissues," *Biomechanics and modeling in mechanobiology*, vol. 15, no. 3, pp. 479–496, 2016.

[28] M. Ambati, T. Gerasimov, and L. De Lorenzis, "A review on phase-field models of brittle fracture and a new fast hybrid formulation," *Computational Mechanics*, vol. 55, no. 2, pp. 383–405, 2015.

[29] J.-Y. Wu, "A unified phase-field theory for the mechanics of damage and quasi-brittle failure," *Journal of the Mechanics and Physics of Solids*, vol. 103, pp. 72–99, 2017.

[30] C. Steinke and M. Kaliske, "A phase-field crack model based on directional stress decomposition," *Computational Mechanics*, vol. 63, no. 5, pp. 1019–1046, 2019.

[31] J. Parmigiani and M. Thouless, "The roles of toughness and cohesive strength on crack deflection at interfaces," *Journal of the Mechanics and Physics of Solids*, vol. 54, no. 2, pp. 266–287, 2006.

[32] T.-T. Nguyen, D. Waldmann, and T. Q. Bui, "Role of interfacial transition zone in phase field modeling of fracture in layered heterogeneous structures," *Journal of Computational Physics*, vol. 386, pp. 585–610, 2019.

[33] M. Paggi and J. Reinoso, "Revisiting the problem of a crack impinging on an interface: a modeling framework for the interaction between the phase field approach for brittle fracture and the interface cohesive zone model," *Computer Methods in Applied Mechanics and Engineering*, vol. 321, pp. 145–172, 2017.

[34] A. C. Hansen-Dörr, R. de Borst, P. Hennig, and M. Kästner, "Phase-field modelling of interface failure in brittle materials," *Computer Methods in Applied Mechanics and Engineering*, vol. 346, pp. 25–42, 2019.

[35] C. Kuhn and R. Müller, "A discussion of fracture mechanisms in heterogeneous materials by means of configurational forces in a phase field fracture model," *Computer Methods in Applied Mechanics and Engineering*, vol. 312, pp. 95–116, 2016.

[36] H. Ming-Yuan and J. W. Hutchinson, "Crack deflection at an interface between dissimilar elastic materials," *International journal of solids and structures*, vol. 25, no. 9, pp. 1053–1067, 1989.

[37] Z. Suo and J. W. Hutchinson, "Interface crack between two elastic layers," *International Journal of Fracture*, vol. 43, no. 1, pp. 1–18, 1990.

[38] J. W. Hutchinson and Z. Suo, "Mixed mode cracking in layered materials," *Advances in applied mechanics*, vol. 29, pp. 63–191, 1991.

[39] S. Li, J. Wang, and M. Thouless, "The effects of shear on delamination in layered materials," *Journal of the Mechanics and Physics of Solids*, vol. 52, no. 1, pp. 193–214, 2004.

[40] D. Leguillon and E. Martin, "The strengthening effect caused by an elastic contrast—part I: the bimaterial case," *International journal of fracture*, vol. 179, no. 1, pp. 157–167, 2013.

[41] D. Leguillon and E. Martin, "The strengthening effect caused by an elastic contrast—part II: stratification by a thin stiff layer," *International journal of fracture*, vol. 179, no. 1, pp. 169–178, 2013.

[42] M. Hossain, C.-J. Hsueh, B. Bourdin, and K. Bhattacharya, "Effective toughness of heterogeneous media," *Journal of the Mechanics and Physics of Solids*, vol. 71, pp. 15–32, 2014.

[43] C. Hsueh, L. Avellar, B. Bourdin, G. Ravichandran, and K. Bhattacharya, "Stress fluctuation, crack renucleation and toughening in layered materials," *Journal of the Mechanics and Physics of Solids*, vol. 120, pp. 68–78, 2018.

[44] S. Brach, M. Hossain, B. Bourdin, and K. Bhattacharya, "Anisotropy of the effective toughness of layered media," *Journal of the Mechanics and Physics of Solids*, vol. 131, pp. 96–111, 2019.

[45] P. Li, J. Yvonnet, C. Combescure, H. Makich, and M. Nouari, "Anisotropic elastoplastic phase field fracture modeling of 3D printed materials," *Computer Methods in Applied Mechanics and Engineering*, vol. 386, p. 114086, 2021.

[46] P. Li, J. Yvonnet, and Y. Wu, "Improved fracture resistance of 3D-printed elasto-plastic structures with respect to their topology and orientation of deposited layers," *International Journal of Mechanical Sciences*, vol. 220, p. 107147, 2022.

[47] J. Xiao, H. Liu, and T. Ding, "Finite element analysis on the anisotropic behavior of 3D printed concrete under compression and flexure," *Additive Manufacturing*, vol. 39, p. 101712, 2021.

[48] T. Daungwilailuk, P. Pheinsusom, and W. Pansuk, "Uniaxial load testing of large-scale 3D-printed concrete wall and finite-element model analysis," *Construction and Building Materials*, vol. 275, p. 122039, 2021.

[49] D. H. Murcia, M. Genedy, and M. R. Taha, "Examining the significance of infill printing pattern on the anisotropy of 3D printed concrete," *Construction and Building Materials*, vol. 262, p. 120559, 2020.

[50] T. T. Le, S. A. Austin, S. Lim, R. A. Buswell, R. Law, A. G. Gibb, and T. Thorpe, "Hardened properties of high-performance printing concrete," *Cement and Concrete Research*, vol. 42, no. 3, pp. 558–566, 2012.

[51] T. Ding, J. Xiao, S. Zou, and X. Zhou, "Anisotropic behavior in bending of 3D printed concrete reinforced with fibers," *Composite Structures*, vol. 254, p. 112808, 2020.

[52] A. R. Arunothayan, B. Nematollahi, R. Ranade, S. H. Bong, J. G. Sanjayan, and K. H. Khayat, "Fiber orientation effects on ultra-high performance concrete formed by 3D printing," *Cement and Concrete Research*, vol. 143, p. 106384, 2021.

[53] B. Zareiyan and B. Khoshnevis, "Effects of interlocking on interlayer adhesion and strength of structures in 3D printing of concrete," *Automation in Construction*, vol. 83, pp. 212–221, 2017.

[54] L. He, H. Li, W. T. Chow, B. Zeng, and Y. Qian, "Increasing the interlayer strength of 3D printed concrete with tooth-like interface: An experimental and theoretical investigation," *Materials & Design*, vol. 223, p. 111117, 2022.

[55] V. N. Nerella, S. Hempel, and V. Mechtcherine, "Effects of layer-interface properties on mechanical performance of concrete elements produced by extrusion-based 3D-printing," *Construction and Building Materials*, vol. 205, pp. 586–601, 2019.

[56] L. Pham, G. Lu, and P. Tran, "Influences of printing pattern on mechanical performance of three-dimensional-printed fiber-reinforced concrete," *3D Printing and Additive Manufacturing*, vol. 9, no. 1, pp. 46–63, 2022.

[57] G. Ji, J. Xiao, P. Zhi, Y.-C. Wu, and N. Han, "Effects of extrusion parameters on properties of 3D printing concrete with coarse aggregates," *Construction and Building Materials*, vol. 325, p. 126740, 2022.

[58] L. Gebhard, J. Mata-Falcon, A. Anton, B. Dillenburger, and W. Kaufmann, "Structural behaviour of 3D printed concrete beams with various reinforcement strategies," *Engineering Structures*, vol. 240, p. 112380, 2021.

[59] L. Pham, P. Tran, and J. Sanjayan, "Steel fibres reinforced 3D printed concrete: Influence of fibre sizes on mechanical performance," *Construction and Building Materials*, vol. 250, p. 118785, 2020.

[60] G. Ma, Z. Li, L. Wang, F. Wang, and J. Sanjayan, "Mechanical anisotropy of aligned fiber reinforced composite for extrusion-based 3D printing," *Construction and Building Materials*, vol. 202, pp. 770–783, 2019.

[61] J. Xiao, Z. Chen, T. Ding, and S. Zou, "Bending behaviour of steel cable reinforced 3D printed concrete in the direction perpendicular to the interfaces," *Cement and Concrete Composites*, vol. 125, p. 104313, 2022.

[62] M. Liu, Q. Zhang, Z. Tan, L. Wang, Z. Li, and G. Ma, "Investigation of steel wire mesh reinforcement method for 3D concrete printing," *Archives of Civil and Mechanical Engineering*, vol. 21, pp. 1–18, 2021.

[63] M. van den Heever, F. Bester, J. Kruger, and G. van Zijl, "Mechanical characterisation for numerical simulation of extrusion-based 3D concrete printing," *Journal of Building Engineering*, vol. 44, p. 102944, 2021.

[64] J. Kruger and J.-P. van der Westhuizen, "Investigating the poisson ratio of 3D printed concrete," *Applied Sciences*, vol. 13, no. 5, p. 3225, 2023.

[65] B. Zhu, J. Pan, Z. Zhou, and J. Cai, "Mechanical properties of engineered cementitious composites beams fabricated by extrusion-based 3D printing," *Engineering Structures*, vol. 238, p. 112201, 2021.

[66] Y. Zhang and F. Aslani, "Development of fibre reinforced engineered cementitious composite using polyvinyl alcohol fibre and activated carbon powder for 3D concrete printing," *Construction and Building Materials*, vol. 303, p. 124453, 2021.

[67] J.-Y. Wu, "A unified phase-field theory for the mechanics of damage and quasi-brittle failure," *Journal of the Mechanics and Physics of Solids*, vol. 103, pp. 72–99, 2017.

[68] B. Bourdin, G. A. Francfort, and J.-J. Marigo, "Numerical experiments in revisited brittle fracture," *Journal of the Mechanics and Physics of Solids*, vol. 48, no. 4, pp. 797–826, 2000.

[69] C. Kuhn, A. Schlüter, and R. Müller, "On degradation functions in phase field fracture models," *Computational Materials Science*, vol. 108, pp. 374–384, 2015.

[70] M. Ghasabeh, *Computational modeling of thermal and shrinkage-induced cracking in concrete*. PhD thesis, Middle East Technical University, 2021.

[71] J.-Y. Wu, V. P. Nguyen, C. T. Nguyen, D. Sutula, S. Sinaie, and S. P. Bordas, "Phase-field modeling of fracture," *Advances in applied mechanics*, vol. 53, pp. 1–183, 2020.

[72] M. Alnæs, J. Blechta, J. Hake, A. Johansson, B. Kehlet, A. Logg, C. Richardson, J. Ring, M. E. Rognes, and G. N. Wells, "The FEniCS project version 1.5," *Archive of numerical software*, vol. 3, no. 100, 2015.

[73] J. Ahrens, B. Geveci, and C. Law, "ParaView: An end-user tool for large data visualization," *Visualization Handbook*, 01 2005.

[74] A. T. Vermeltfoort, T. Raijmakers, and H. Janssen, "Shear tests on masonry walls," 1993.

[75] P. J. B. B. Lourenço, *Computational strategies for masonry structures.* PhD thesis, Technische Universiteit Delft, 1996.

[76] K. Chaimoon and M. M. Attard, "Modeling of unreinforced masonry walls under shear and compression," *Engineering structures*, vol. 29, no. 9, pp. 2056–2068, 2007.

[77] C. Xu, C. Xiangli, and L. Bin, "Modeling of influence of heterogeneity on mechanical performance of unreinforced masonry shear walls," *Construction and Building Materials*, vol. 26, no. 1, pp. 90–95, 2012.

[78] A. Costa, "Experimental testing of lateral capacity of masonry piers. An application to seismic assessment of AAC masonry buildings," *Universitat degli Studi di Pavia*, 2007.